Structural and morphological changes of breast cancer cells induced by iron (II) complexes

Janske Nel, David Siniscalco, Cécilia Hognon, Mathilde Bouché, Nadège Touche, Emilie Brunner, Philippe Gros, Antonio Monari, Stéphanie Grandemange, Gregory Francius

▶ **To cite this version:**

Janske Nel, David Siniscalco, Cécilia Hognon, Mathilde Bouché, Nadège Touche, et al.. Structural and morphological changes of breast cancer cells induced by iron (II) complexes. Nanoscale, 2022, 14 (7), pp.2735-2749. 10.1039/D1NR08301E . hal-03563765

HAL Id: hal-03563765
https://hal.science/hal-03563765

Submitted on 21 Oct 2022

HAL is a multi-disciplinary open access archive for the deposit and dissemination of scientific research documents, whether they are published or not. The documents may come from teaching and research institutions in France or abroad, or from public or private research centers.

L'archive ouverte pluridisciplinaire **HAL**, est destinée au dépôt et à la diffusion de documents scientifiques de niveau recherche, publiés ou non, émanant des établissements d'enseignement et de recherche français ou étrangers, des laboratoires publics ou privés.

Structural and Morphological Changes of Cancer Cells Induced by Iron (II) Complexes

Janske Nel [a†], David Siniscalco [b†], Cécilia Hognon [c†], Mathilde Bouché [d], Nadége Touche [e], Émilie Brunner [e], Philippe C. Gros [d], Antonio Monari [c, f*], Stéphanie Grandemange [e*], Grégory Francius [b*]*

[a] Université de Lorraine, LIBio, F-54000, Nancy, France

[b] Université de Lorraine and CNRS. LPCME UMR 7564, F-54000 Nancy, France

[c] Université de Lorraine and CNRS, LPCT UMR 7019, F-54000 Nancy, France

[d] Université de Lorraine and CNRS, L2CM UMR 7053, F-54000, Nancy, France

[e] Université de Lorraine and CNRS, CRAN UMR 7039, F-54000 Nancy, France

[f] Université de Paris, ITODYS, CNRS, F-75006, Paris, France

[†] These authors contributed equally to this work

[*] Corresponding authors

KEYWORDS: Breast cancer cell lines, metallodrugs, iron-based complexes, biological membranes, AFM, molecular dynamics.

ABSTRACT

Metal-based complexes are well-established cancer chemotherapeutic agents. Although our knowledge regarding their exact activity *vs* toxicity profile is incomplete, changes in cell membrane biophysical properties and cytoskeletal structures have been implicated as part of their mechanism of action. Thus, in this work, we examine the influence of iron-based complexes on the structural and morphological properties of epithelial non-tumorigenic (MCF 10A) and tumorigenic (MDA-MB-231) breast cell lines using atomic force microscopy (AFM), flow cytometry and immunofluorescence microscopy. At 24 h of exposure, both the MCF 10A and MDA-MB-231 cells underwent a cell softening, and an increase in size and granulometry, followed by a re-stiffening at 96 h. MDA-MB-231 underwent a notable cytoskeletal and mitochondrial reorganization with increased actin stress fibers and cell-to-cell communication structures, ruffling at cell leading edges, larger more disperse networks of mitochondria, and large structures within the cytoplasm. An extensive all-atom molecular dynamic simulation suggests a possible direct and unassisted internalization of the metallodrug, and confirmed that the cellular effects could not be ascribed to the simple physical interaction of the iron-based complexes with the biological membrane. These observations provide an insight into a link between the mechanisms of action of iron-based complexes as anti-cancer treatment and cytoskeletal architecture.

While metal-based complexes have achieved indisputable success as anti-cancer agents, as the well-known use of cisplatin to treat various solid tumors proves, their use is plagued with drug resistance and severe side effects that limit their efficacy and diminish patient quality of life. [1–3] Historically, the development of novel anti-cancer metal-based drug candidates has been focused on noble or rare metals such as ruthenium, gold and rhodium, [4–6] but recently the possibility of using iron has gained prominence.[7] Iron, an essential cofactor in a number of enzymatic and physiological processes, is considered an alternative anti-cancer metal-based complex due to its biocompatibility and relatively lower toxicity as compared to non-essential metals. In 1978, Fiorina et al. reported the low but significant anti-cancer activity of ferrocenyl compounds against lymphocytic leukemian [8] and, ever since, a multitude of ferrocene derivatives with structural and mechanistic diversity have been developed for various therapeutic applications. [9,10] Notably, among the ferrocene derivatives, the ferrocifens are the most widely studied due to their potential to suppress both hormone dependent and independent breast cancer cells. [11–14]

The development of novel anti-cancer iron-based metallodrugs, including ferrocene and its derivatives, [15,16] have necessitated a thorough understanding of the behaviour and modes of action of metal-based drugs. Indeed, there is a need to unravel the chemical- and molecular-based phenomena from those induced at the cellular level in both healthy and cancerous cells.

Such considerations are crucial for metal-based complexes as, although their bioavailability is limited due to limited solubility and cell internalization, they have a large action spectrum and are able to interact with various cellular components and biological macrostructures to induce both direct effects (such as oxidative stress induction) and indirect effects based on cell signaling activation. [6,17–19]

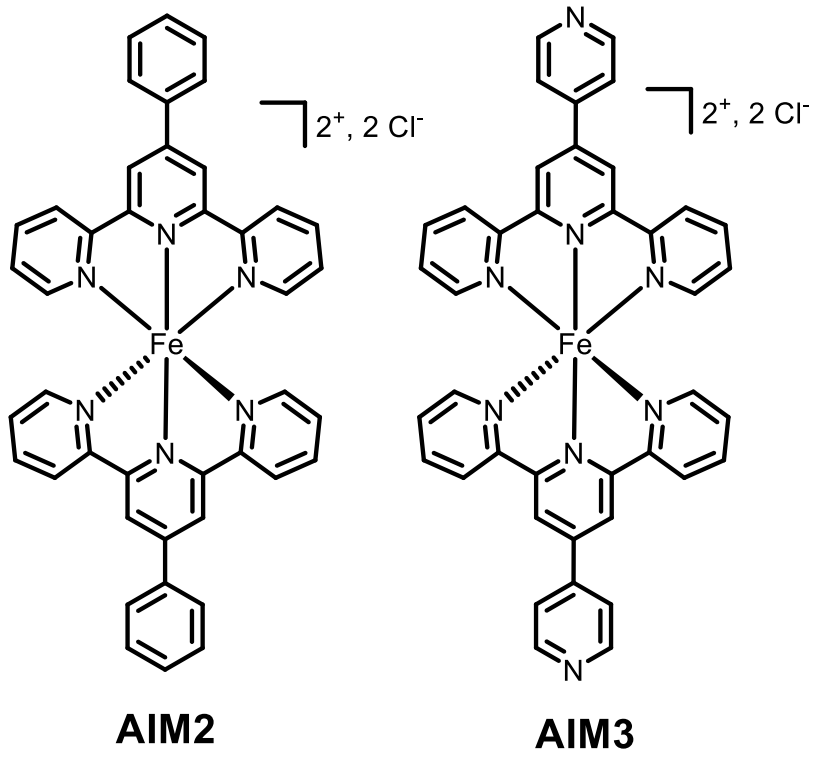

Figure 1. Molecular structure of AIM 2 and AIM 3. Note the peripheral phenyl or pyridyl moiety differentiating the two components.

Previously, we have demonstrated that iron-II polypyridyl compounds bearing peripheral phenyl or pyridine groups, hereafter denoted as AIM (anti-cancer iron molecule) 2 or AIM 3 (**Figure 1**), were able to form persistent aggregates with DNA *via* groove binding and intercalation, and induce a significant decrease in cell proliferation at 2 µM treatment. [20] This interaction with DNA is promising as it justifies a potential anti-cancer capacity of the compounds. Notably, AIM 2 and AIM 3 complexes were synthesized according to our reported procedure. [20] Their stability over 72 h incubation at 37 °C in both aqueous media and fetal bovine serum was confirmed by UV-vis spectroscopy and HPLC. Some polypyridyl-ruthenium complexes tend to aggregate in aqueous media as highlighted by Gasser et al., [21] and similarly millimolar concentrations of AIM tend to aggregate in water. However, UV-vis spectroscopy confirmed that

neither AIM 2 nor AIM 3 showed aggregation under the conditions used herein, *i.e.* at 2µM concentration in aqueous media, hence preventing bias in experiments further detailed herein see Figure S1 in Supplementary Information).

In this contribution, we explored the effects of AIM 2/3 on the rigidity and cytoarchitecture of non-tumorigenic and tumorigenic cell lines *via* the use of atomic force microscopy (AFM), flow cytometry and immunofluorescence confocal microscopy on MCF 10A and MDA-MB-231 cells. These cell lines were chosen for their distinguishing features; MCF 10A cells are adherent, non-transformed, display a lack of tumorigenicity in nude mice, a lack of anchorage-independent growth, and a dependence on growth factors.[22] In contrast, MDA-MB-231 cells form highly malignant, invasive tumors *in vivo*, are resistant to chemotherapy drugs such as paclitaxel, [23] exhibit anchorage-independent growth, and grow independently of growth factors. [24]

Cytoskeletons are internal polymer networks that not only give cells their shape and mechanical strength but through their changes, especially their ability to withstand external and internal pressure, can indicate the health of cells. [25] Indeed, there is increasing evidence of a functional relationship between tissue rigidity and tumor progression. [26] In tumors, studies have shown an increase in tissue rigidity due to several contributing factors; firstly, due to the exacerbated proliferative nature of cancer cells and their ability to evade apoptosis and suppressor genes, the number of cancerous cells increase within a limited space; this is accompanied by increased matrix deposition and interstitial fluid pressure giving rise to increased mechanical force that translates to tissue rigidity. [27] However, this rigidity is not necessarily shared with the individual tumoral cells, as tissue rigidity involves the collective interaction between different cells types, extracellular matrices and proteins. Instead, individual tumoral cells have been found to be more malleable. [28,29]

As a consequence biomechanical properties including cellular stiffness, modulus of elasticity, and adhesion related to cellular cytoarchitecture have been widely investigated using atomic force microscopy (AFM).[30] Thus, in the present contribution our goal is to characterize the effects of the iron metallodrugs on cellular mechanical properties as a biomarker for possible anti-cancer efficiency. To discriminate between the biological- and chemical-based effects of metallodrugs, we studied the interactions of AIM 2/3 with model supported lipid bilayers mimicking biological cell membranes. These results are complemented with the use of extended μs scale molecular dynamic simulations to pinpoint the specific interactions occurring between AIM scaffolds and the lipid bilayer components. Additionally, the characterization of the cytoskeletal architecture, to investigate cell size and granulometry, was performed using flow cytometry, whilst internal structural changes were visualized by immunofluorescence staining. Our multidisciplinary approach, combining physico-chemical analyses and cellular biology assays, allows us to characterize the effects of the AIM 2 and 3 compounds on the cellular morphology and mechanical properties, whilst confirming the possibility of the unassisted internalization of the complexes.

RESULTS AND DISCUSSION

Atomistic simulation of lipid bilayer exposed to metallodrug

For both AIM 2 and AIM 3, the results of the MD simulations describing the interaction with lipid bilayers were similar.

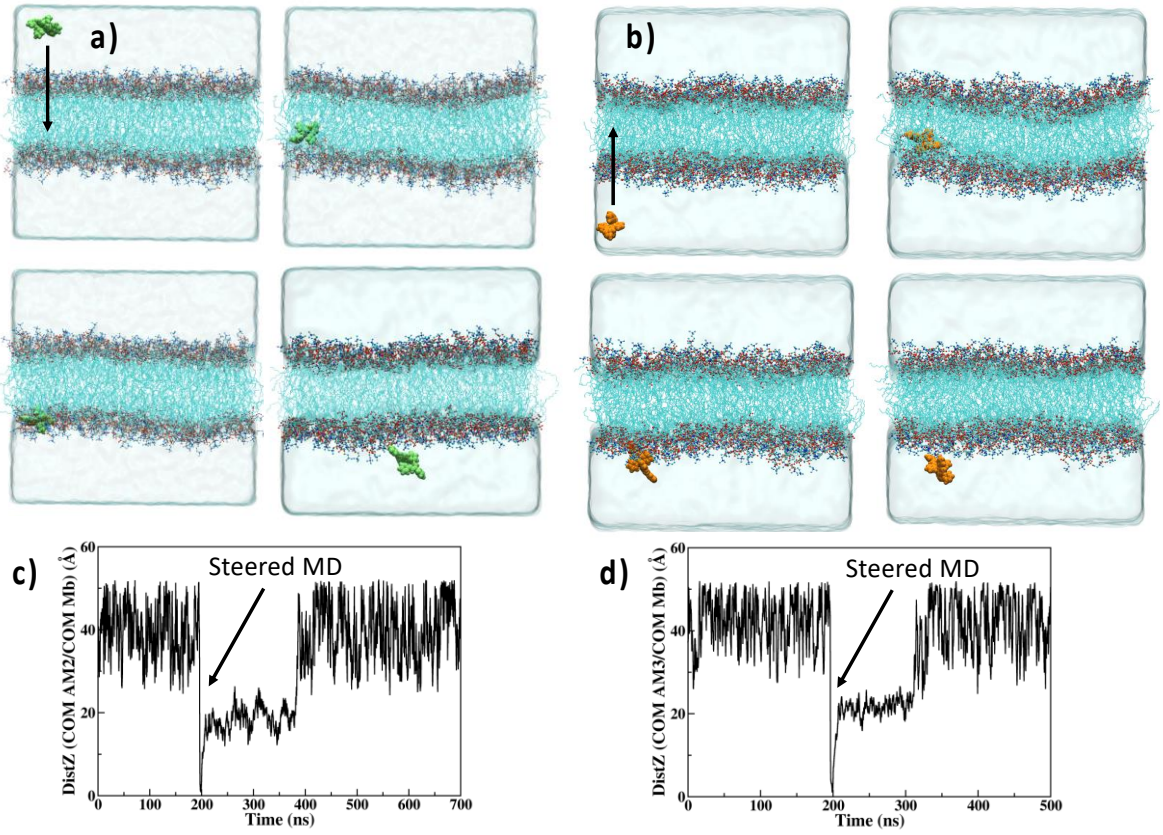

Figure 2. Representative snapshots illustrating the evolution of AIM 2 (**a**, the drug shown in green) and AIM 3 **(b**, the drug shown in orange) after the steered MD to position it in the center of the membrane. The action of the steered MD is exemplified by the black arrow in the first panel of both series. Time series of the position of the center of mass of AIM 2 **(c)** and AIM 3 **(d)** projected on the membrane vertical axes. The time series for the other independent trajectories are given in SI.

As shown in **Figure 2**, we can identify a common pattern; when AIM 2/3 is initially placed in the water bulk, the complex interacts slightly with the polar head region but no spontaneous penetration into the lipid membrane core is observed. However, this internalization process, wherein the molecule enters the core of the membrane, can be forced using a relatively small biasing force of only 1 kcal/mol. Although we have not provided a full free energy profile in relation to the membrane penetration, as that would be outside the scope of the present contribution, we may anticipate that the low value of the biasing force should correlate to the presence of a small energetic barrier. In turn this confirms the possibility that AIM 2/3 accomplishes direct cell internalization through cell membrane penetration without necessitating the assistance of specific transporters. Once the biasing force is relinquished, AIM rapidly leaves the core of the bilayer and positions itself at the polar head region, and more specifically the fatty acid exposed at the interface of the membrane, where it develops a persistent aggregate. This behavior is not unexpected, as AIM 2 is charged and decorated with extended hydrophobic ligands, and its positioning at the interface allows the charge to stabilize while maintaining a favorable network of dispersive and hydrophobic interactions.

The persistence time of the aggregate does not exceed 1 μs, as shown by the time series of the position of AIM center of mass projected on the membrane axis shown in **Figure 2 (c, d)**. Furthermore, in the majority of cases, AIM's polar head aggregate is released causing AIM to be expelled back into the water bulk. Notably, the μs-scale persistency time was only obtained for AIM 2 and the data are not sufficient to extrapolate a difference in behavior between the two metallodrugs. The spontaneous release of AIM from the lipid membrane constitutes a further indication of its possible unassisted internalization. The metastable aggregate and the relatively short, compared to biologically relevant time scales, persistence are also excluding an eventual

accumulation of AIM at the membrane level, which in turn could induce an increase of the membrane rigidity by simple chemical and physical processes. Indeed, only a persistence time reaching macroscopic scales, *i.e.* of the order of seconds, should be sufficient to justify alone a macroscopic alteration of the mechanical properties of the bilayer.

Real-time morphology evolution of supported lipid bilayer exposed to metallodrugs

The morphological changes of the DPPC/POPC (3:1) supported lipid bilayers (SLBs) were monitored in buffer solution at room temperature before and after addition of either AIM 2 or AIM 3, at a final concentration of 50 µM, in the AFM fluid cell. The topographic images of SLB regions at the same location were recorded before and after exposure to the AIM metallodrugs for 30 and 60 minutes as shown in **Figure 3**.

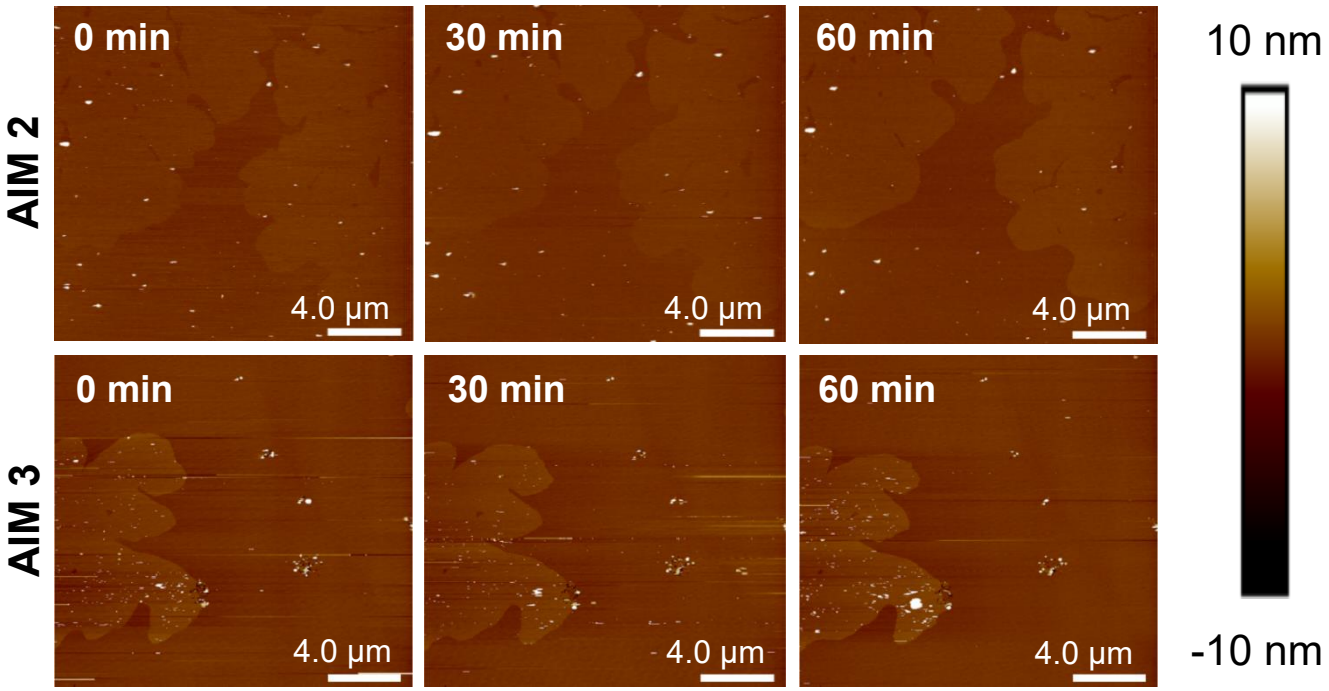

Figure 3. AFM images monitoring the real time evolution of DPPC/POPC SLB under the effects of either AIM 2 or AIM 3 after 0, 30 and 60 mins. Image scale bar is set to 4 µm.

Before exposure of the metallodrugs, the AFM images of native DPPC/POPC (3:1) SLB recorded in buffer solution showed the coexistence of two phases, wherein the lighter and darker levels correspond to DPPC- and POPC-enriched phases, respectively. The step height measured between the two phases was approximately 1.5 ±0.5 nm (see vertical cross-sections in Figure S2) and resulted from a difference in the thickness and mechanical properties of the DPPC and POPC layers. After 30 minutes of exposure to either metallodrug, DPPC/POPC SLB morphology remained unaltered, even after 60 min whatever the metallodrugs even if the concentration is extremely high (about 20 times the dose concentration used for tumoral cells treatment). We noticed a slight accumulation of aggregates over time at the SLB surface, especially when it was exposed to AIM 3. Such aggregation at the SLB surface without any significant modifications of SLBs domains was low and not clearly visible on all AFM imaging sequences but could be related to the high drug concentration. The absence of membrane damage or modifications are coherent with the results of the MD simulations which highlighted only transient aggregates having a sub-μs persistence time and excluded the accumulation of the drug at the membrane. Indeed, it consistently appears that the hydrophobic forces acting on the AIM metallodrugs are not sufficient to lock them within the SLB, instead AIM can almost freely cross the membrane establishing an equilibrium between the medium bulk and the mica surface. As a matter of fact, a space of few nm, corresponding to 3 up to 5 water layers, is present between the SLB and the mica substrate allowing the establishment of the aforementioned equilibrium.

Nanomechanical effect of metallodrugs on non-tumorigenic and tumorigenic cell lines as measured by AFM

The stiffness distribution for MCF 10A (**Figure 4**) and MDA-MB-231 (**Figure 5**) were measured for cells treated with AIM 2 or AIM 3 after 24 and 96 h and compared to untreated controls. Cell stiffness was calculated from the theoretical fittings of experimental force curves using the Sneddon model as illustrated by Figure S3 in the Supporting Information. As the experimental force curves were continuous, without any different elasticity regimes, we provide only the global values for the whole cells and not for each organelle, such as the nucleus, mitochondria or cytoplasm. The change in cell stiffness distribution was analyzed for both cell lines as a shift in their median and mean kPa (**Table 1**). Notably, our stiffness measurements for MCF 10A and MDA-MB-231 matches that of literature, in that non-tumorigenic cell lines (*i.e.* MCF 10A) are stiffer than tumorigenic cell lines (*i.e.* MDA-MB-231).[32–35]

Table 1. AFM nanomechanical stiffness (kPa) median and mean values for MCF 10A and MDA-MB-231 cells after 24 or 96 h with either no treatment (control), treatment with AIM 2 or AIM 3.

MCF 10A			**MDA-MB-231**		
	24 h			**24 h**	
Treatment	**Median (kPa)**	**Mean (kPa)**	**Treatment**	**Median (kPa)**	**Mean (kPa)**
Control	6.85	8.64 ±6.81	Control	3.92	5.43 ±4.57
AIM 2	2.66	4.84 ±4.96	AIM 2	3.55	4.62 ±4.06
AIM 3	1.04	2.80 ±4.01	AIM 3	2.69	4.00 ±4.03
	96 h			**96 h**	
Treatment	**Median (kPa)**	**Mean (kPa)**	**Treatment**	**Median (kPa)**	**Mean (kPa)**
Control	6.92	8.23 ±4.95	Control	4.44	5.93 ±6.15
AIM 2	6.32	7.27 ±4.59	AIM 2	2.36	5.62 ±8.88
AIM 3	2.78	4.53 ±4.29	AIM 3	3.62	6.29 ±8.19

For untreated non-tumorigenic MCF 10A cells, cell stiffness is stable from 6.85 to 6.92 kPa from 24 to 96 (**Figure 4, a & d**). Following 24 h of AIM 2 treatment, however, cell stiffness decreases significantly as compared to control (6.85 vs 2.66 kPa, $P < 0.050$). Similarly, AIM 3

also cause a significant decrease in cell stiffness compare to control untreated cells (6.85 vs 1.04 kPa, $P < 0.050$) (**Figure 4, b & c**). Interestingly, although AIM 2 treatment softens the cells after 24 h, they stiffen again at 96 h to reach almost the same kPa as the control (6.32 vs 6.92 kPa). A similar trend was noted for AIM 3; a softening of the cells at 24 h followed by a re-stiffening at 96 h (1.04 at 24 h and 2.78 kPa at 96 h), however, in this case, the cells were still much softer than the control at 96 h (6.92 vs 2.78 kPa) (**Figure 4, e & f**). Altogether, not only does AIM 2 and AIM 3 cause significant differences to MCF 10A cell stiffness but the metallodrugs also caused different stiffness effects on the cells (AIM 2 vs AIM 3, $P < 0.050$).

A cell stiffening over time was observed for the untreated tumorigenic MDA-MB-231 cells, wherein the stiffness increased from 3.92 to 4.44 kPa from 24 to 96 h (**Figure 5, a & d**). Following 24 h of AIM 2 treatment, a small but significant decrease in cell stiffness was observed (3.92 vs 3.55 kPa, $P < 0.050$). Treatment with AIM 3 for 24 h also caused a significant decrease in cell stiffness as compared to the control (3.92 vs 2.69 kPa, $P < 0.050$) (**Figure 5, b & c).** After 96 h, untreated MDA-MB-231 cells stiffened from 3.92 to 4.44 kPa. Interestingly, AIM 2 treatment caused a continual cell softening from 24 to 96 h (3.55 to 2.36 kPa) (**Figure 5, b & e**) whilst AIM 3 followed a similar pattern as the control; an initial softening at 24 h followed by a stiffening after 96 h (2.69 to 3.62 kPa) (**Figure 5, c & f**). Altogether, AIM 2 appeared to have the most significant effect on MDA-MB-231 cells causing the cells to soften notably from 24 to 96 h (**Table 1**).

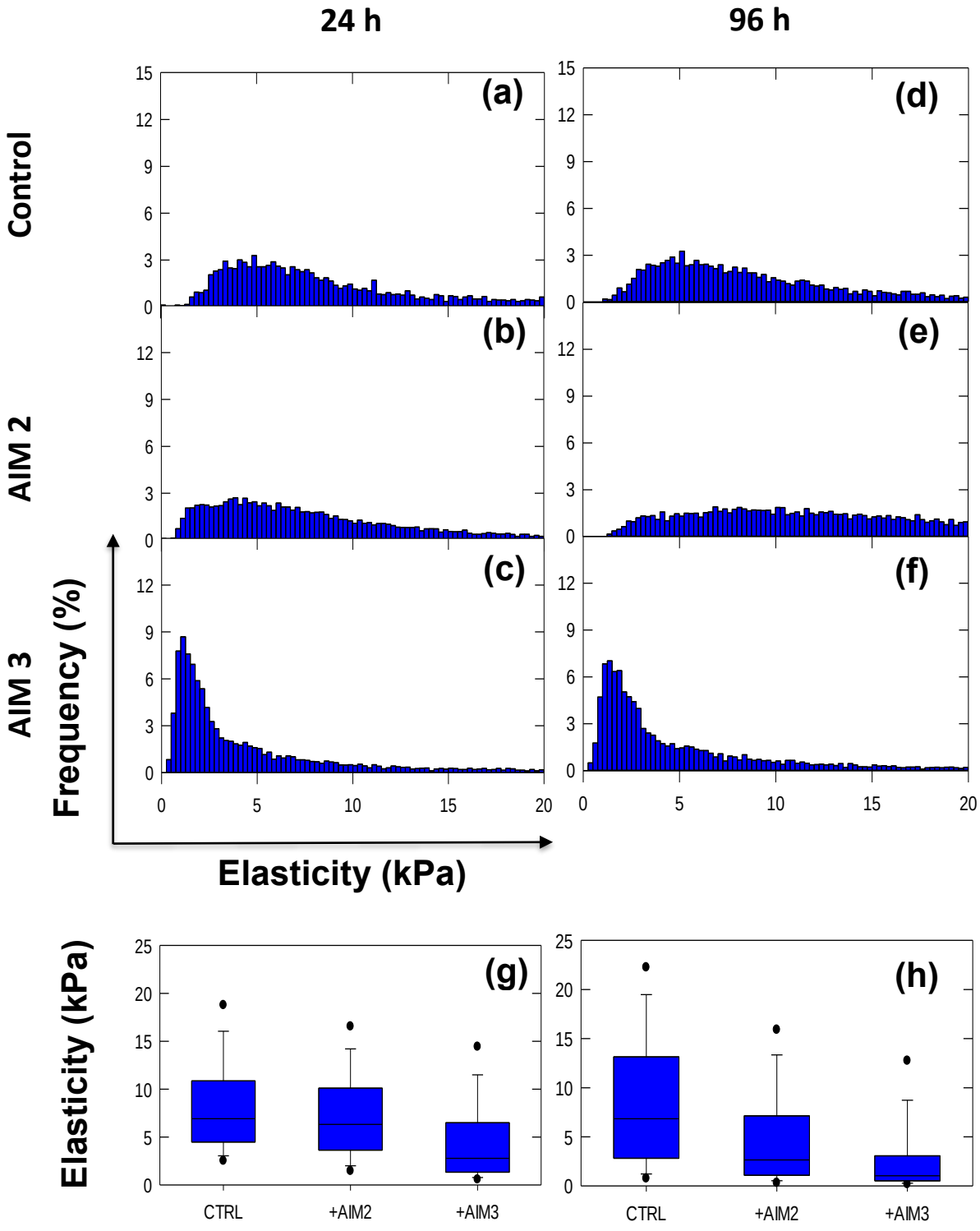

Figure 4. AFM nanomechanical measurements of stiffness (kPa) distribution on MCF 10A cells after 24 h (**a – c**) and 96 h (**d – f**) with either no treatment (**a, d**), treatment with 2 μM AIM 2 (**b, e**) or AIM 3 (**c, f**). A box-and-whisker plot indicating the shift in median elasticity (kPa) of MDA-MB-231 cells from no treatment (control) and treatment with either AIM 2 or AIM 3 at 24 (**g**) and 96 h (**h**) is also indicated.

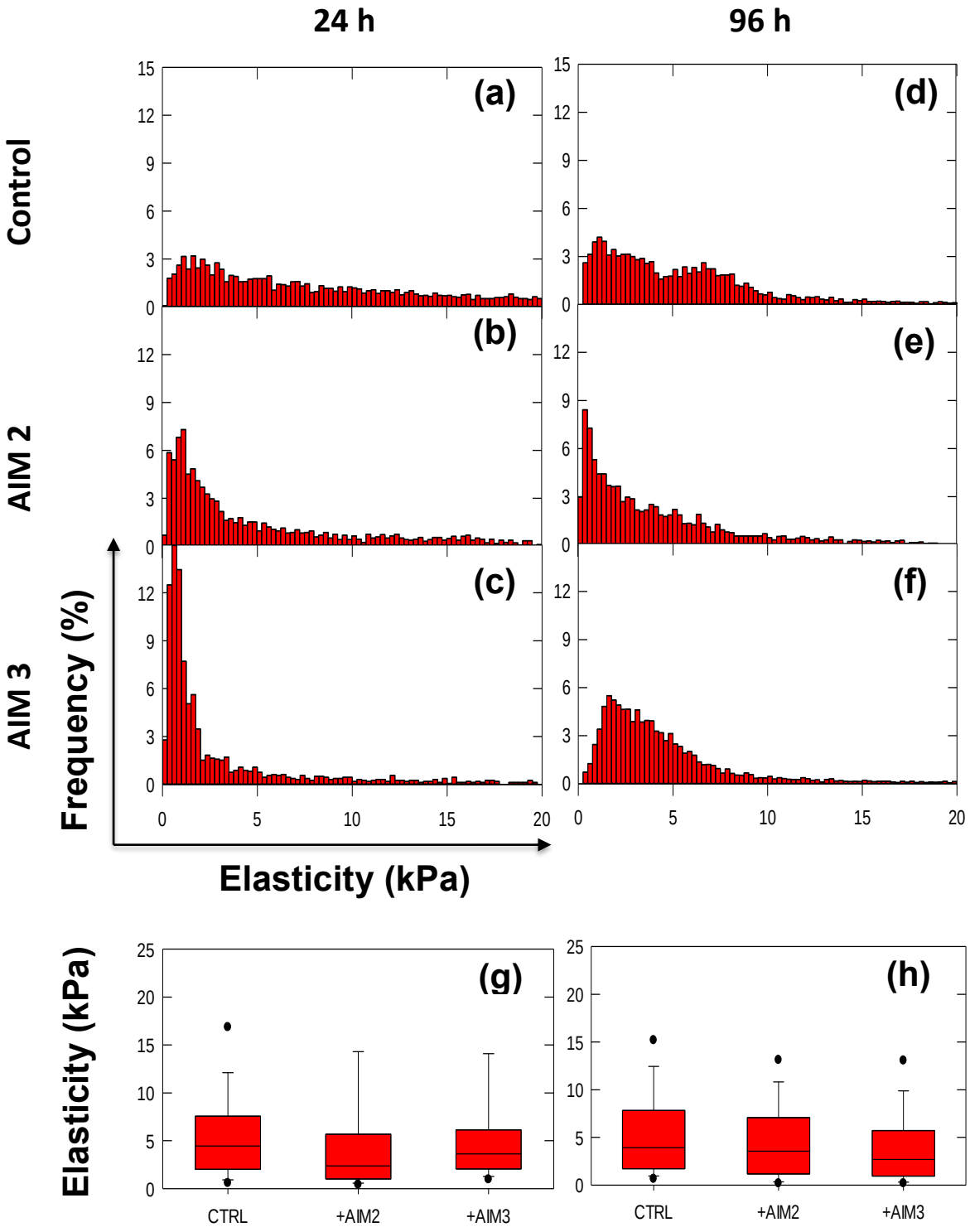

Figure 5. AFM nanomechanical measurements of stiffness (kPa) distribution on MDA-MB-231 cells after 24 h (**a – c**) and 96 h (**d – f**) with either no treatment (**a, d**), treatment with 2 µM AIM 2 (**b, e**) or AIM 3 (**c, f**). A box-and-whisker plot indicating the shift in median elasticity (kPa) of MDA-MB-231 cells from no treatment (control) and treatment with either AIM 2 or AIM 3 at 24 (**g**) and 96 h (**h**) is also indicated.

Morphological effect of metallodrugs on non-tumorigenic and tumorigenic cell lines as measured by AFM

AFM morphological imaging was performed to characterize and compare cellular morphology properties to the nanomechanical changes observed previously. MCF 10A (**Figure 6**) and MDA-MB-231 (**Figure 7**) cells were treated with either the AIM 2 or AIM 3 metallodrug for 24 and 96 h, and were compared to non-treated cells of a similar time frame.

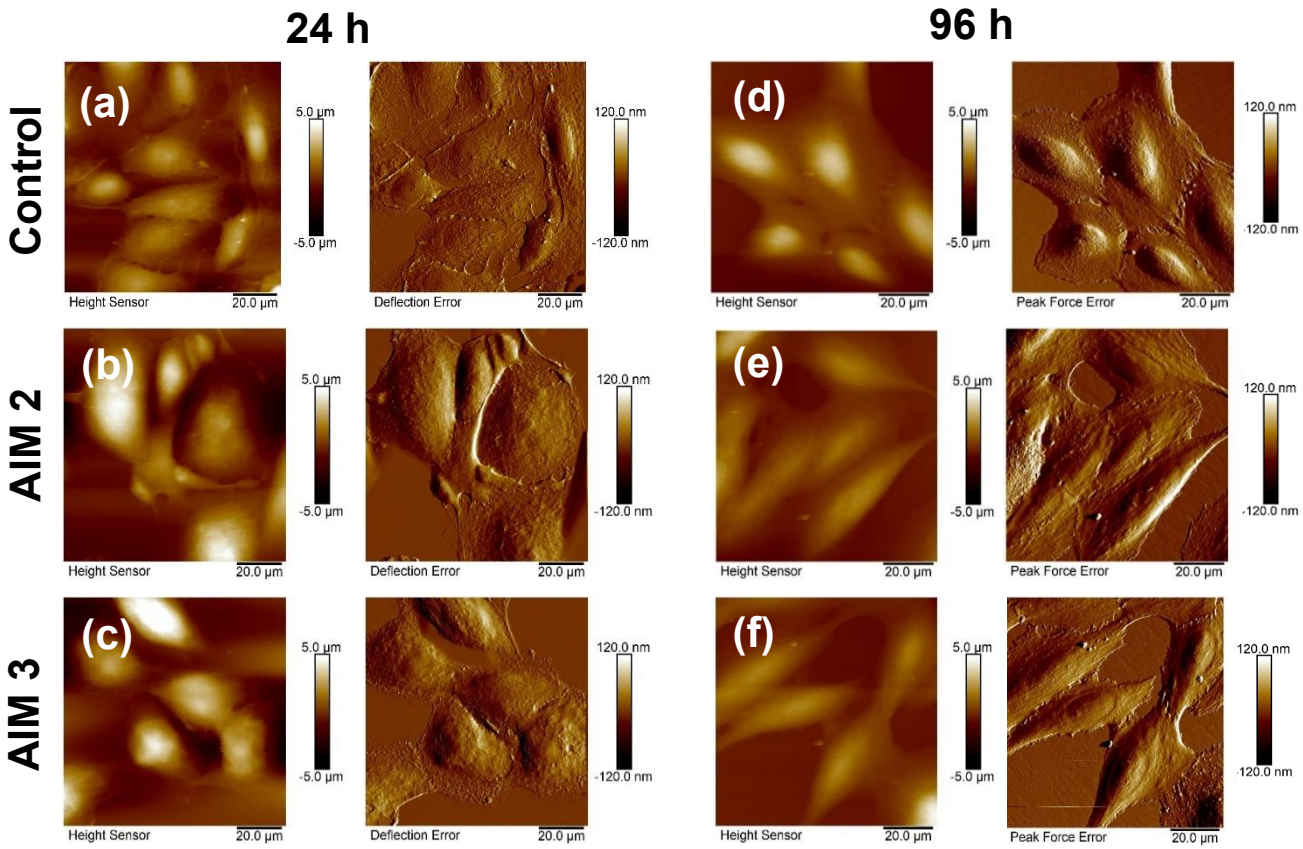

Figure 6. AFM morphological images on MCF 10A cells after 24 h **(a – c)** and 96 h **(d – f)** with either no treatment **(a & d)**, treatment with AIM 2 **(b & e)** or AIM 3 **(c & f)**. The first and third columns show the height sensor images and the second and fourth columns show the peak force error images. Image scale bar is set to 20 µm.

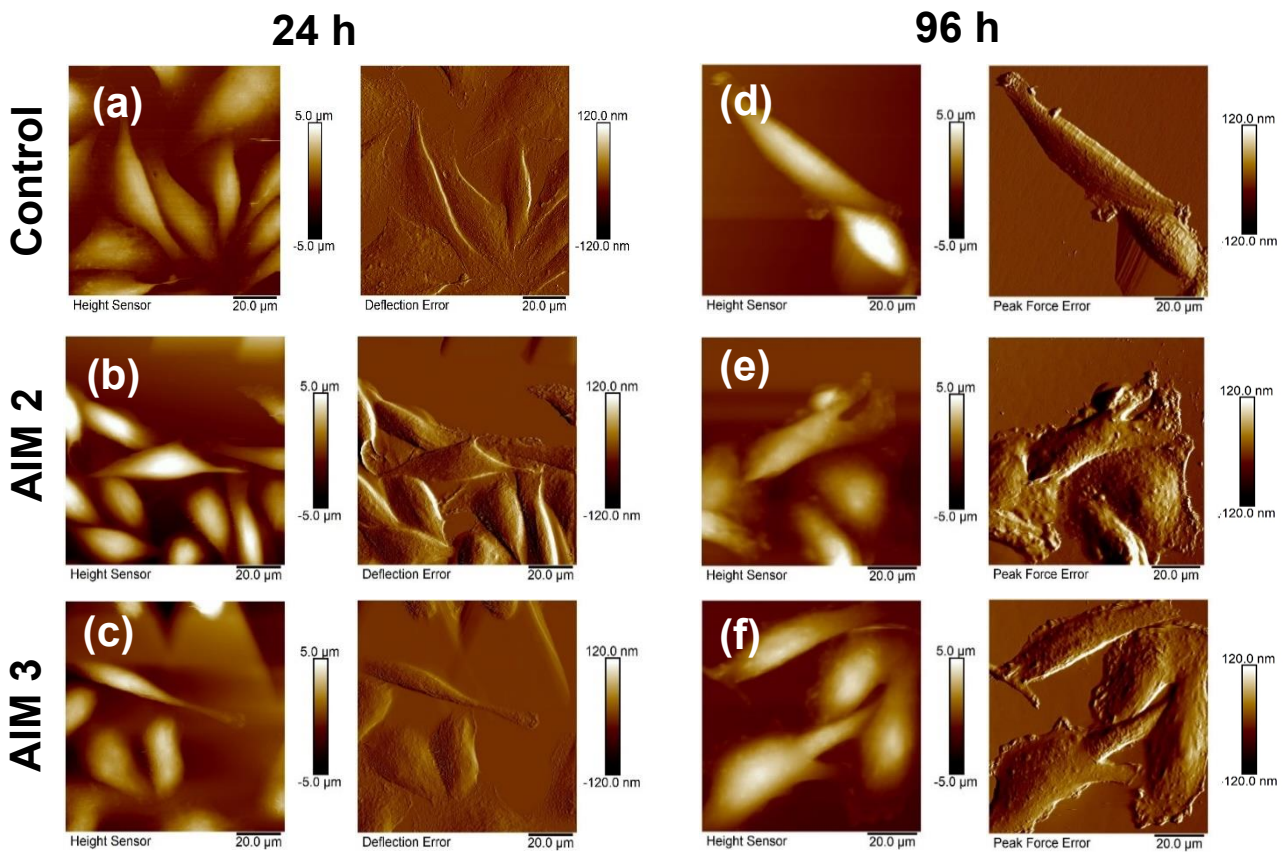

Figure 7. AFM morphological images on MDA-MB-231 cells after 24 h (**a – c**) and 96 h (**d – f**) with either no treatment (**a & d**), treatment with 2 µM AIM 2 (**b & e**) or AIM 3 (**c & f**). The first and third columns show the height sensor images and the second and fourth columns show the corresponding peak force error images. Image scale bar is set to 20 µm.

At 24 and 96 h, untreated MCF 10A cells had a similar polygonal or cobblestone appearance characteristic of epithelial cells (**Figure 6, a & d**). When treated with AIM 2, the cells become more elongated from 24 to 96 h (**Figure 6, b & e**). AIM 3 caused a similar elongation of the cells from 24 to 96 h (**Figure 6, c & f**) with a rounding of the cells at 24 h (**Figure 6, c**).

Untreated MDA-MB-231 cells grew in distinct spindle-like shapes at 24 and 96 h which is characteristic for this cell line (**Figure 7, a & d**). With AIM 2 treatment, the MDA-MB-231 cells increased in height and became slightly rounder at 24 h (**Figure 7, b**). At 96 h, the cells appeared slightly larger with cell edge ruffling (**Figure 7, e**). Similarly, with AIM 3 treatment, the MDA-MB-231 cells increased in height from 24 to 96 h and displayed cell edge ruffling (**Figure 7, c & d**).

Analysis of cell size and granulometry using flow cytometry

Considering our results from MD simulations and SLB experiments, wherein we observed that only metastable aggregates have been identified by MD simulations with no noticeable change in the properties of the SLB recorded, we conclude that the metallodrugs penetrate into the internal structure. Hence, we can safely exclude that the differences in the mechanical properties of the membranes are due to the simple accumulation of the drugs at the membrane. The difference in cellular stiffness and morphology should be a result of the metallodrugs altering cellular architecture and/or signaling pathways by associating with the cellular membrane, cytoskeleton, nucleus or organelles which in turn could have an impact on the cell size and complexity within the cell. To further explore these observations, we performed flow cytometry analyses on both cell lines at 24 and 96 h after either AIM 2 or AIM 3 treatment to determine if a quantifiable size and complexity difference could be discerned.

The cell size and granulometry of MCF 10A (**Figure 8**) and MDA-MB-231 (**Figure 9**) were measured for untreated and treated with AIM 2 or AIM 3 after 24 and 96 h. With flow cytometry analysis, an increase in FSC is commonly interpreted as a cell size increase, whilst an increase in the SSC is interpreted as an increase in the granulometry, or complexity, within the cell.

The change in cell size and granulometry was analysed as a percentage shift in the population after applying a threshold. This threshold was the same for both cell lines and served to exclude debris. Normalized percentages of the populations (**Figure 10**), after thresholding, were calculated using each cell line's median population at either 24 or 96 h (**Table 2**).

Table 2. Flow cytometry results, before percentage normalization, indicating the effect of AIM 2 and AIM 3 on the size and granulometry of MCF 10A and MDA-MB-231 after 24 or 96 h. All experiments were performed in triplicate. Results acquired as x 10^4.

MCF 10A			**MDA-MB-231**		
Size (mean, ±SD)			**Size (mean, ±SD)**		
Treatment	**24 h**	**96 h**	**Treatment**	**24 h**	**96 h**
Control	186.35 ±3.42	167.93 ±2.89	Control	188.46 ±6.07	183.45 ±0.87
AIM 2	238.14 ±11.19	312.14 ±6.32	AIM 2	221.46 ±3.88	197.60 ±6.27
AIM 3	229.45 ±4.58	272.95 ±55.81	AIM 3	223.40 ±5.32	198.86 ±2.96
Granulometry (mean, ±SD)			**Granulometry (mean, ±SD)**		
Treatment	**24 h**	**96 h**	**24 h**	**96 h**	**Treatment**
Control	15.44 ±0.34	21.71 ±0.54	Control	14.46 ±0.73	18.17 ±0.05
AIM 2	25.97 ±0.95	47.97 ±1.49	AIM 2	19.61 ±0.81	27.17 ±0.52
AIM 3	23.15 ±0.50	47.60 ±1.93	AIM 3	20.10 ±0.44	27.59 ±1.36

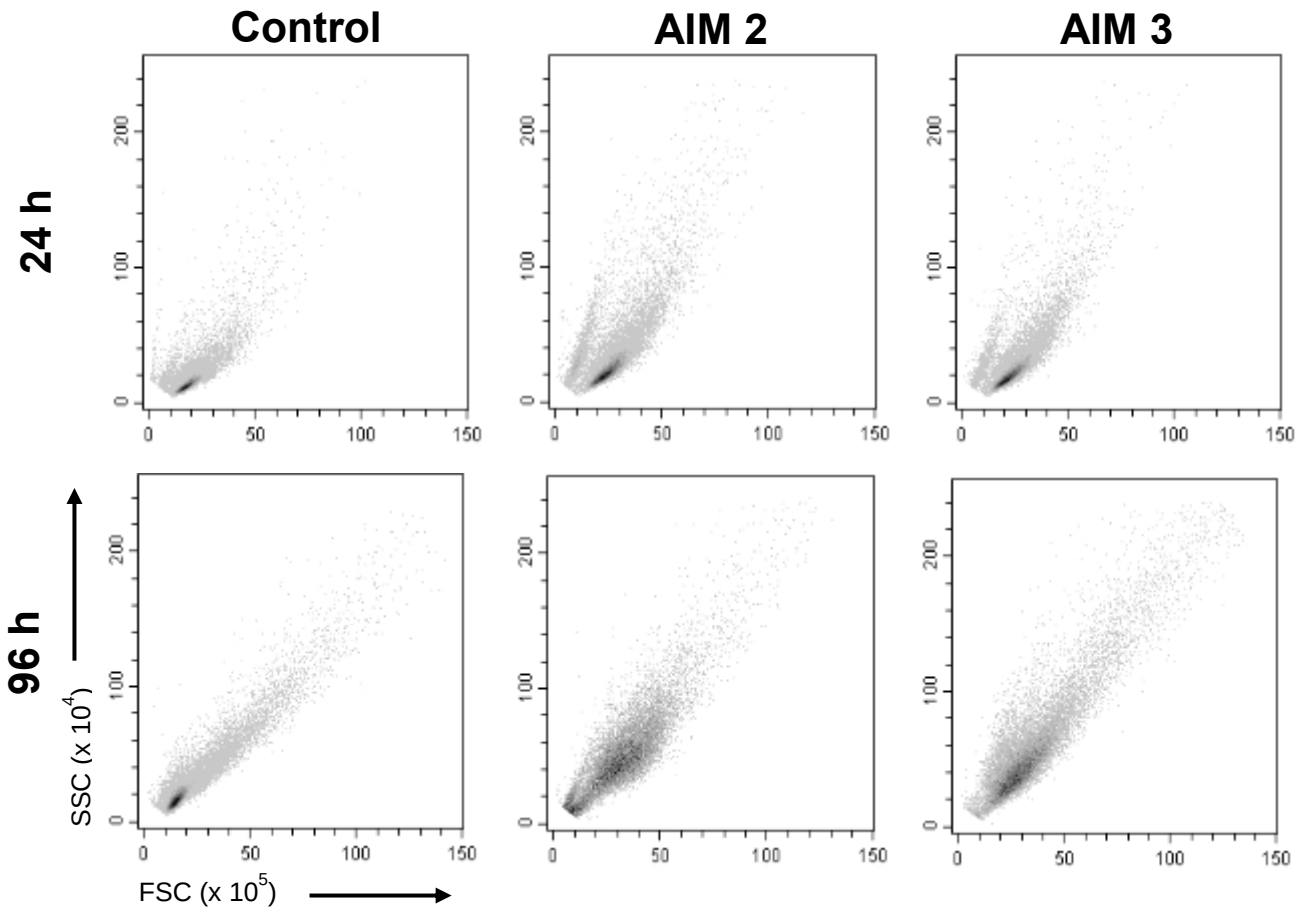

Figure 8. Examples of the flow cytometry forward (size) vs. side scatter (granulometry) intensity plots of MCF 10A at 24 h and 96 h with either no treatment (control), treatment with 2 μM AIM 2 or treatment with AIM 3. All intensity plots are shown after application of a threshold which included all living cells, whilst dots at less than 10 x 10^5 in the forward scatter area (FSC-A) and 20 x 10^4 side scatter area (SSC-A) were considered debris and were removed from the population.

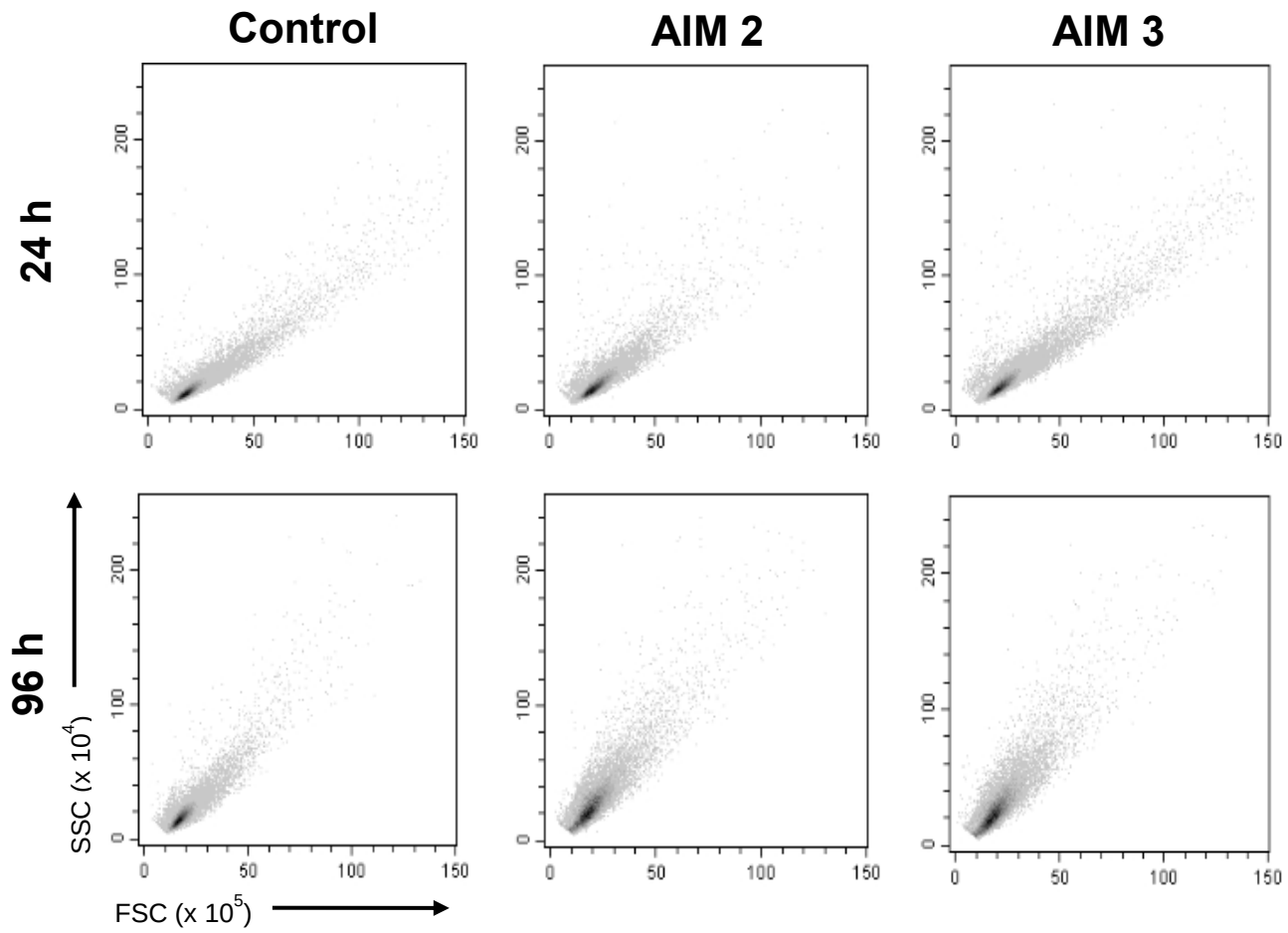

Figure 9. Examples of the flow cytometry forward (size) vs. side scatter (granulometry) intensity plots of MDA-MB-231 at 24 h and 96 h with either no treatment (control), treatment with AIM 2 or treatment with AIM 3. All intensity plots are shown after application of a threshold which included all living cells, whilst dots at less than 10 x 10^5 in the forward scatter area (FSC) and 20 x 10^4 side scatter area (SSC) were considered as debris and were removed from the population.

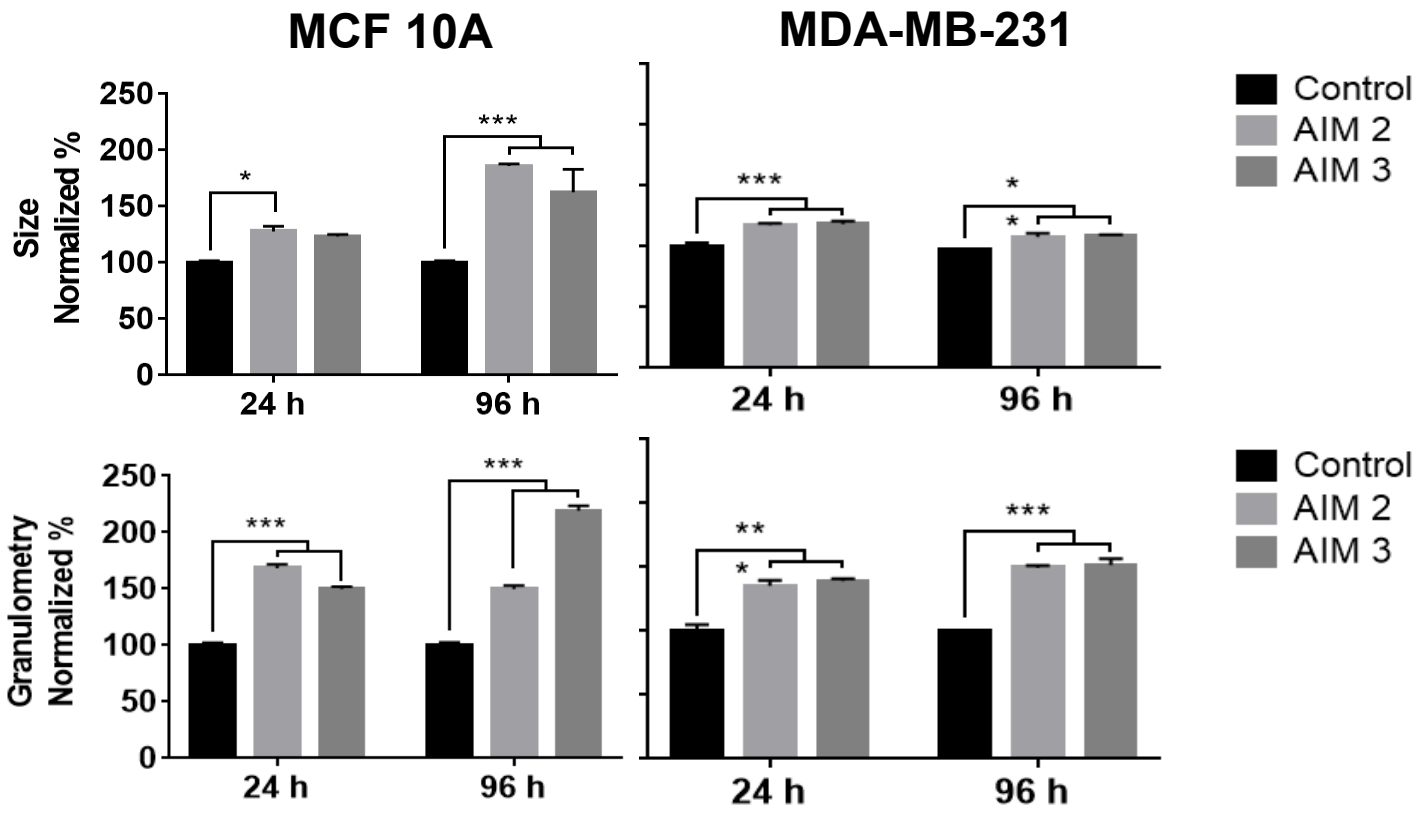

Figure 10. The effect of iron-based complexes on the size and granulometry of MCF 10A and MDA-MB-231 cells. Cells were treated with 2 μM AIM 2 or AIM 3 for 24 or 96 h and analyzed by flow cytometry to determine the effect of the metallodrugs on the size and granulometry of MCF 10A or MDA-MB-231. Results are shown as normalized percentage with ±SD with untreated cells at each time point used as 100 %.

For untreated non-tumorigenic MCF 10A cells, the population's cell size decreased 9.89 % from 24 to 96 h whilst the granulometry increased 40.56 % (**Table 2**). Following AIM 2 treatment, however, the population's cell size increased significantly with 27.79 % after 24 h (P = 0.0476) and 85.88 % after 96 h ($P < 0.0001$) as compared to controls**.** Granulometry also increased markedly during this time; 68.15 % after 24 h ($P < 0.0001$) and 121.00 % after 96 h ($P < 0.0001$)

(**Figure 10**). With AIM 3 treatment, there was a 23.13 % increase in size which was not significantly different from control (P = 0.1037) but a significant increase of 49.91 % in granulometry after 24 h ($P < 0.0001$) was noted. After 96 h with AIM 3 treatment, the population's cell size and granulometry increased significantly by 62.54 % ($P < 0.0001$) and 119.32 % ($P < 0.0001$), respectively, as compared to controls (**Figure 10**). Notably, both AIM 2 and AIM 3 had a similar change in the population's cell size at both 24 h (AIM 2 vs AIM 3, P = 0.8943) and 96 h (P = 0.1448). AIM 2 had a greater effect on MCF 10A granulometry however at 24 h (AIM 2 vs AIM 3, P = 0.029) than at 96 h (AIM 2 vs AIM 3, P = 0.9162).

For untreated MDA-MB-231 cells, the population's cell size decreased by 2.66 % from 24 to 96 h whilst the granulometry increased 25.64 % (**Table 2**). Following AIM 2 treatment, however, the size of the cells within the population increased significantly after 24 h by 17.51 % ($P < 0.0001$) and after 96 h by 7.71 % (P = 0.0074) as compared to controls at the same time points. Similarly, granulometry also increased significantly during this time; 35.58 % after 24 h ($P < 0.0001$) and 49.50 % after 96 h ($P < 0.0001$) (**Figure 10**). With AIM 3 treatment, there was also a significant increase in the population's cell size (18.54 %, $P < 0.0001$) and granulometry (38.98 %, $P < 0.0001$) after 24 h. After 96 h with AIM 3 treatment, the population's cell size increased 8.40 % (P = 0.0041) and the granulometry increased 51.84 % ($P < 0.0001$) as compared to controls (**Figure 10**). In the tumorigenic MDA-MB-231 cell line, AIM 2 and AIM 3 had a similar effect at 24 h and 96 h on cell size (AIM 2 vs AIM 3, P = 0.8671 and P 0.9410) and granulometry (AIM 2 vs AIM 3, P = 0.7165 and 0.7796), respectively.

Analysis of cellular structure using immunofluorescence confocal microscopy

Due to these prominent external changes, we decided to further explore the internal effect of the iron-based complex treatment on MCF 10A and MDA-MB-231 cells by immunofluorescent microscopy to enable the visualization of the cell cytoskeleton (F-actin and α-tubulin), mitochondria, and nucleus. α-Tubulin was stained to visualize the cytoskeleton of the cells, specifically microtubule organization. Microtubules are involved in cellular movement, including cytoplasmic transport of membrane vesicles and organelles, chromosome alignment during meiosis/mitosis, nerve-cell axon migration, etc. As previously noted with our AFM morphological studies, untreated MCF 10A cells displayed their characteristic cobblestone-like growth pattern with organized α-tubulin architecture (**Fig. 11, a – d**). Following 24 h of AIM 2 treatment, cell appearance appeared unchanged (**Fig. 11, e & f**), however at 96 h the cells displayed more irregular, elongated shapes (**Fig. 11, g & h**). AIM 3 treatment had a similar effect and caused the MCF 10A cells to grow in more irregular, elongated shapes at 96 h (**Fig. 11, k – l**). For untreated MDA-MB-231 cells, their characteristic spindle-like growth was apparent at 24 and 96 h (**Fig. 11, m – p**). Both AIM 2 and AIM 3 treatment caused the cells to be noticeably larger after 24 h (**Fig. 11, q – r & u – v**). At 96 h the cells were more irregular in shape, and exhibited microtubule and α-tubulin disorganization (**Fig. 11, s – t & w – x**). This disorganization was not noted for MCF 10A. Interestingly, in MDA-MB-231 cells both AIM 2 and AIM 3 treatments caused an increase in the number of filopodia and thin, long structures similar to tunneling nanotubes (**Fig. 11, q, s, u, w & x**).

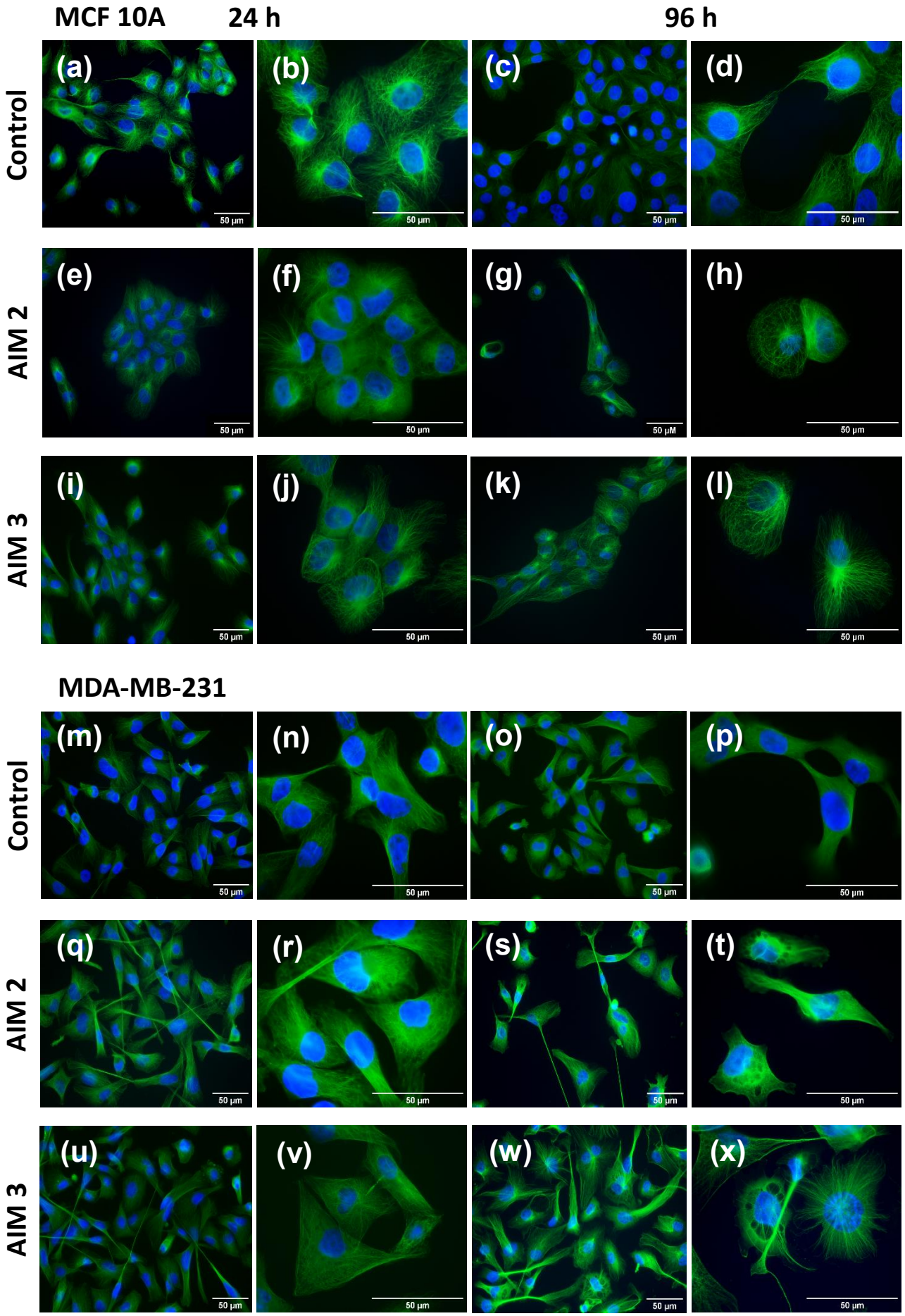

Figure 11. Immunofluorescence microscopy images on MCF 10A (**a – l**) and MDA-MB-231 (**m – x**) cells after 24 h **(columns 1 & 2)** and 96 h **(columns 3 & 4)** at 40X or 100X magnification. Cellular α-tubulin (green) and DNA (blue) was stained after either no treatment **(a – d & m – p, respectively)**, treatment with AIM 2 **(e – h & q – t, respectively)** or AIM 3 **(i – l & u – x, respectively)**. Image scale bar is set to 50 µm.

Actin, another essential component of the cell cytoskeleton, provides stability and morphogenesis to cells, and is involved in crucial processes such as cell division, endocytosis and cell migration. For untreated MCF 10A cells, the F-actin fibers were structured as expected with some filopodia and lamellipodia formation (**Fig. 12, a – d**). However, after 24 h of AIM 2 or AIM 3 treatment, the cells presented with more stress fibers, lamellipodial extensions and dense, unidirectional actin networks at their leading edges (**Fig. 12, e – f & i – j**). The effect was similar at 96 h after treatment with AIM 2 or AIM 3, where after the cells had prominent stress fibers and dense actin networks (**Fig. 12, g – h & k – l**). For untreated MDA-MB-231 cells at 24 and 96 h, highly organized F-actin fibers were observed (**Fig. 12, n & p**). At 24 and 96 h of AIM 2 treatment, however, the F-actin was more focused at the outside edges of the cells with increased stress fibers (**Fig. 12, q – r & s – t**). With AIM 3 treatment at 24 and 96 h, the cells were distinctly irregularly-shaped with cell edge ruffling, and increased filopodia, lamellipodia, stress fibers and structures similar to tunneling nanotubes (**Fig. 12, u & w**).

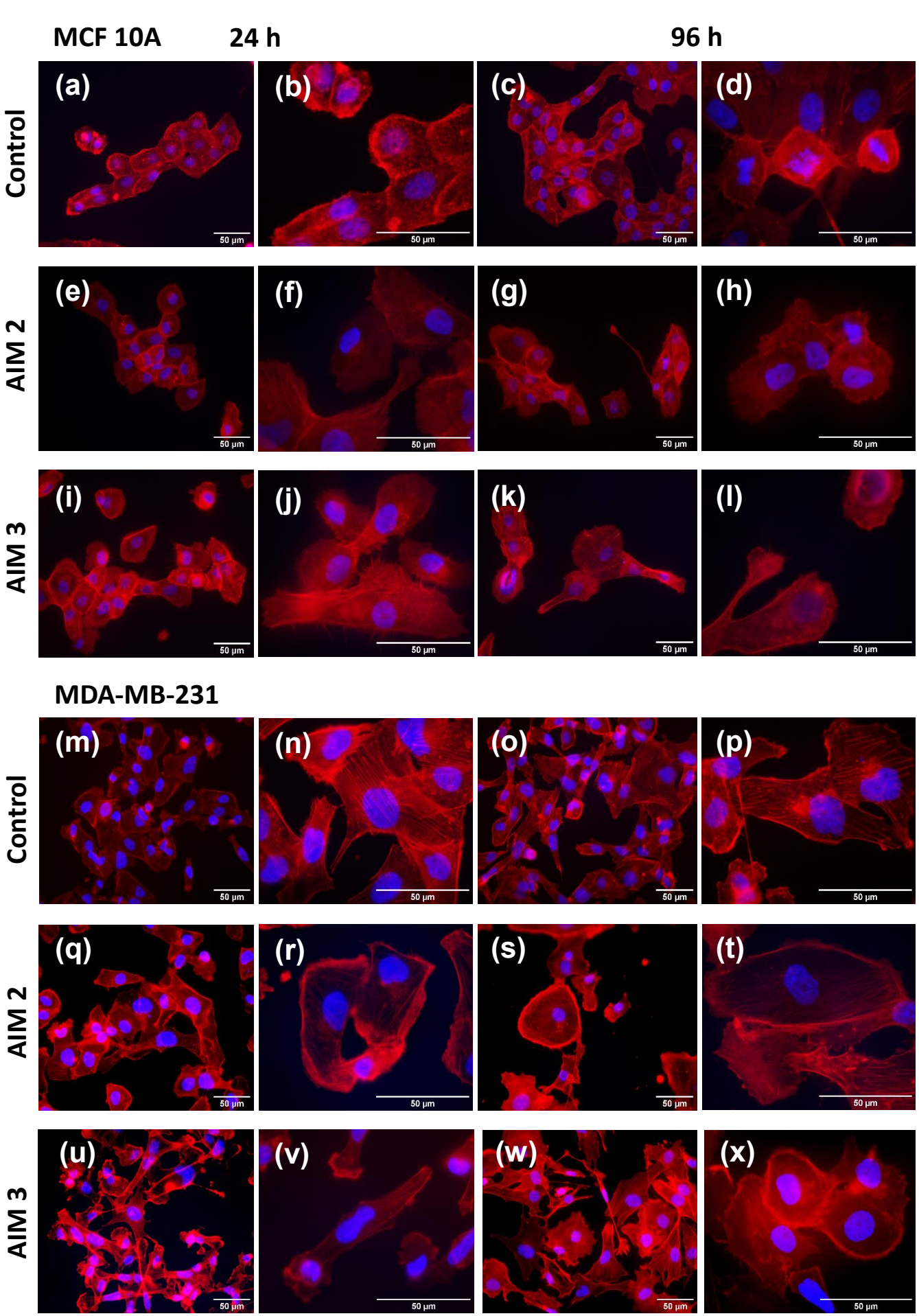

Figure 12. Immunofluorescence microscopy images on MCF 10A (**a – l**) and MDA-MB-231 (**m – x**) cells after 24 h **(columns 1 & 2)** and 96 h **(columns 3 & 4)** at 40X or 100X magnification. Cellular F-actin (red), and DNA (blue) was stained after either no treatment **(a – d & m – p, respectively)**, treatment with AIM 2 **(e – h & q – t, respectively)** or AIM 3 **(i – l & u – x, respectively)**. Image scale bar is set to 50 µm.

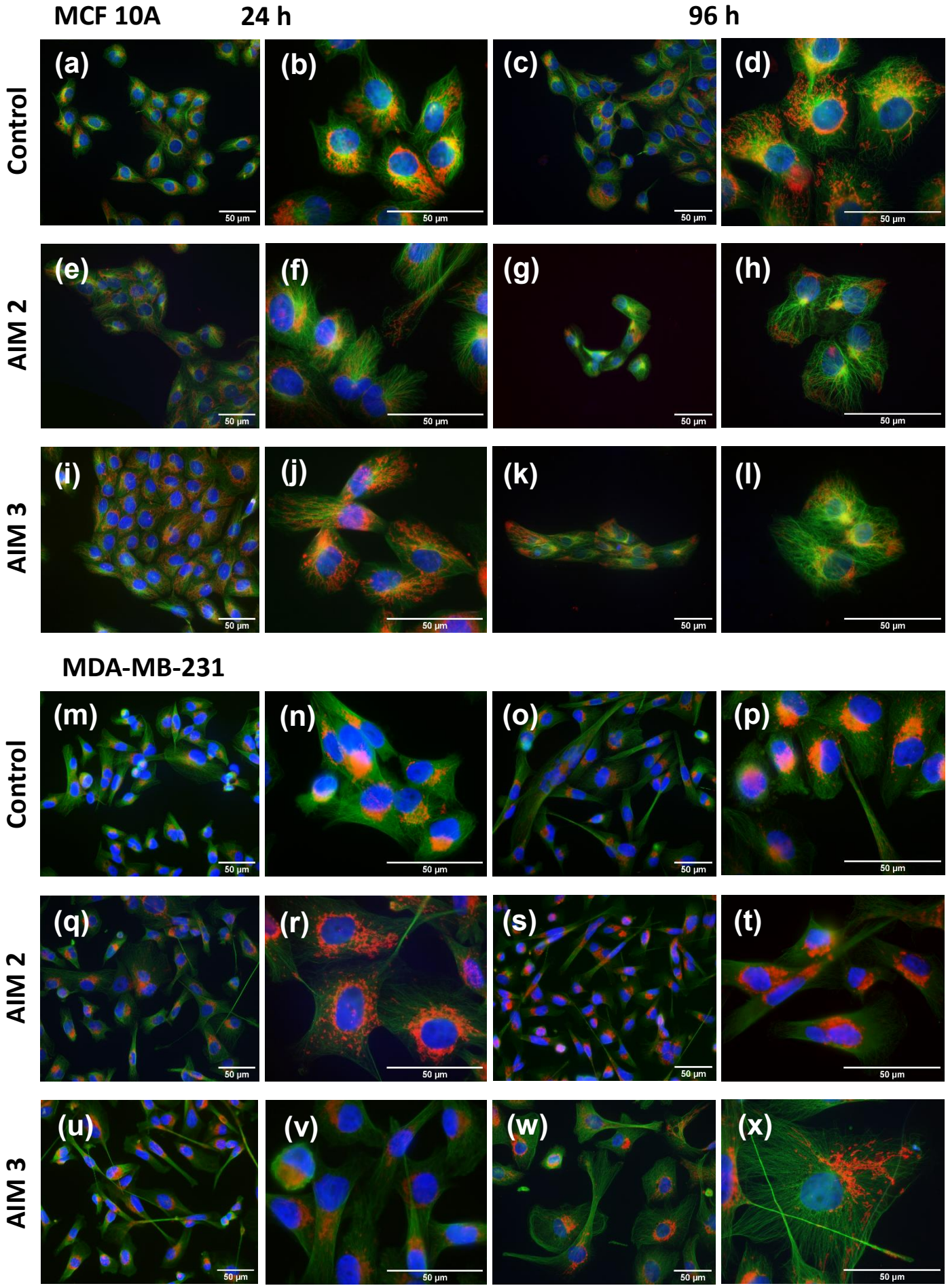

Figure 13. Immunofluorescence microscopy images on MCF 10A (**a – l**) and MDA-MB-231 (**m – x**) cells after 24 h **(columns 1 & 2)** and 96 h **(columns 3 & 4)** at 40X or 100X magnification. Cellular α-tubulin (green), cytochrome c (red), and DNA (blue) was stained after either no treatment **(a – d & m – p, respectively)**, treatment with AIM 2 **(e – h & q – t, respectively)** or AIM 3 **(i – l & u – x, respectively)**. Image scale bar is set to 50 µm.

The fluorescent staining of α-tubulin and cytochrome c of MCF 10A (**Fig. 13, a – l**) and MDA-MB-231 (**Fig. 13, m – x**) showed a clear difference in the mitochondrial arrangement between treated and untreated cells. Untreated MCF 10A cells displayed organized cytoskeletal structures with dispersed mitochondrial filamentous networks centered around the nucleus (**Fig. 13, a – d**). A similar cytoskeletal and mitochondrial arrangement was observed after 24 h of AIM 2 and 3 treatment, although the mitochondrial networks appeared more fragmented with AIM 3 (**Fig. 3, e & f and i & j**). However, after 96 h both AIM 2 and 3 treatment caused a distinct change in the mitochondrial networks in the cells; instead of being centered mostly around the nucleus, the mitochondria were observed near both the nucleus and the leading edges of the cells (**Fig. 13, g & h and k & l**). This could be a stress response due to the iron-based complex treatment leading to the development of stress fibers and lamellipodial extensions. [36] Studies have also implicated a change in mitochondrial arrangement, wherein the mitochondria migrate to the focal adhesion points of cells, to promote motility. [37] In a 1D environment, MCF 10A cells are known to travel three times faster than MDA-MB-231 cells, however, MDA-MB-231 cells travel farther which is consistent with the metastatic potential of the cell lines. [38] Using a wound healing assay (see Figure S4 and Figure S5 in the Supplementary Information), we ascertained that neither 24 nor 72 h AIM 2/3 treatment caused an increase in the metastatic potential of either cell line, rather the monolayer scratches were filled due to proliferation rather than the migration of cells.

For untreated MDA-MB-231 cells, the cytoskeleton appeared well organized with mitochondria appearing in a distinct cluster to one side of the nucleus (**Fig. 13, m – p**) which coincides with literature [36,39,40]. After 24 h of AIM 2 treatment, larger and more disperse networks of mitochondria were observed (**Fig. 13, q & r**) which subsided after 96 h (**Fig. 13, s & t**). With AIM 3 treatment at 24 h, although the mitochondria were to one side of the nucleus (as in control

cells), the clusters were larger, denser and more fragmented (**Fig. 13, v**). Similarly, at 96 h, large irregularly-shaped cells with large cytoplasmic structures and dense fragmented mitochondrial networks were apparent (**Fig. 13, w & x**). These structures could be the localization of AIM 2/3 in vacuoles within the cell cytoplasm or due to interaction of the metallodrugs with cytoskeleton proteins or matrix metalloproteinase activity[41–45]. These interactions could reduce the metastasis-related properties of triple-negative breast cancer cells such as migration, invasion and re-adhesion.

Thus, AIM 2 treatment causes MCF 10A cells to have irregular, elongated shapes with less microtubule organization. With AIM 3 treatment, there was a similar increase in size of cells, as well as an increase in stress fibers and a distinct spatial shift of the mitochondrial networks. For MDA-MB-231 cells, AIM 2 and AIM 3 treatments caused; distinct cytoplasmic disorganization; increased cell edge ruffling; and increased filopodia, tunneling nanotube-like structures, and stress fibers. This coincides with previous literature and our AFM nanomechanical results that there is a correlation between cytoskeletal organization and stiffness. [32] Thus, considering the nanomechanical and morphological AFM data, as well as the flow cytometry data, we surmised the following; MCF 10A cells treated with AIM 2 for 24 h were softer, more elongated and were larger and more complex. After 96 h, the cells stiffened (approaching control kPa) but had increased in size and granulometry. After 96 h, the cells had stiffened to almost control kPa, with an elongated shape, and a dramatically increased size and complexity as compared to control. With AIM 3 treatment at 24 h, cells were significantly softer than control, as well as rounder, larger and more complex. After 96 h, the cells stiffened slightly (but did not return to control stiffness), became elongated, and were larger and more complex. MDA-MB-231 cells treated with AIM 2 for 24 h were: softer, rounder, slightly larger, and increased internal complexity. After 96 h, the

cells continued to soften, were larger with increased complexity within the cell. With AIM 3 treatment at 24 h, cells were softer, rounded, and were larger and more complex than controls. At 96 h, cells were stiffening, were slightly larger, and had increased complexity.

Thus, overall, our results indicated that AIM 2 actions on cells mechanical properties seems to depend on the specific cell lines. Metal-based complexes have been shown to affect the organization of cell cytoskeleton and induce changes in the architecture of cytoskeleton networks.[46] The disorganization or modification in the cytoskeleton may come from a biological response of the cells due to a metabolic change as evidenced by changes in the mitochondrial networks of the cells. This assumption is supported by the fact that the AIM complexes do not accumulate within the cell membrane, as observed on SLB and MD simulations, but cross the plasma membrane thus enabling the compounds to interfere with cell metabolism and cytoplasm organization. The latter experiencing a statistically significant decrease of their stiffness upon the effects of the metallodrug while the effects on the former are less evident and generalizable.

Furthermore, the results on model SLB and by MD simulations are excluding that those effects could be due to the simple chemical accumulation of the drug at the membrane interface. Indeed, the AFM images of the treated SLB show no difference with the control, and MD simulations clearly indicated that both drugs only form metastable interactions with the membrane having a permanence time scarcely exceeding the μs time-scale. The MD simulation have also suggested that the metallodrug could be spontaneously internalized through the lipid membrane without necessitating the action of specific carriers, a result highly promising for their possible pharmacological use. These considerations are extremely promising in the framework of combined chemotherapy applications as they point towards the possible use of such compounds as adjuvants or sensitizers.

In regards to the mechanism of action elicited by AIM 2/3, in a previous study we noted that both AIM 2 and AIM 3 had an effect on cell viability. [20] In the same study we ascertained that although the toxicity of iron (II) complexes is often associated with oxidative stress, in the case of AIM 2/3, the iron is strongly protected by the ligand thus no Fenton reaction is induced. Instead, the interaction of the complexes with DNA was evident and could be related to an inhibition in duplication and structural modifications preventing recognition by and interactions with enzymes leading to a change in cellular structure and behaviour. Notably, the mechanisms of action regarding how metal-based drugs induce cytotoxicity are not fully understood and, in most cases, will include a variety of biological targets including nucleic acids, proteins membrane phospholipids, and thiol-containing molecules. [47] Various metals have been thought to have different effects, for example; the mode of action for platinum complexes includes the induction of changes in the structure of nucleic acids due to the increased formation of adducts which may effect replication and transcription resulting in cell death; [48–51] ruthenium has been associated with G2/M cell cycle arrest; and iron-complexes have been speculated to interact with a family of metallo-nuclease enzymes leading to oxidative DNA single-strand breaks. [52] Both chemotherapeutic agents and metal-based complexes interact and have an effect on cancer cell shape, cytoskeletal architecture and the cell cycle, [53–55] and metal-based complexes such as iron have been noted for their ability to inhibit tubulin polymerization and affect microtubule organization. [56–58] Similar effects have been seen with gold, platinum and ruthenium complexes able to target actin polymerization and microtubule networks. [59,60] To be able to provide more exact mechanisms of action for iron-based complexes in cancer therapy, we plan to unravel the precise biological signaling pathways activated and leading to this cytoarchitectural change induced by our iron-based complex treatment.

CONCLUSION

In this contribution we demonstrated the influence of iron-based complexes on the morphological and structural properties of two distinct breast cell lines. Based on the results, we support our initial hypothesis that iron (II)-based complexes affect the cytoarchitecture and intracellular structural rearrangements of cells which lead to global changes in mechanical deformability of the cell. Consequently, complexes such as iron-based metallodrugs, which modify the stiffness of tumoral cells could be promising in improving cancer therapeutics.

MATERIAL AND METHODS

Chemicals

1,2-Dipalmitoyl-*sn*-glycero-3-phosphocholine (DPPC, ≥ 99%), 1-palmitoyl-2-oleoyl-glycero-3-phosphocholine (POPC, ≥ 99%), 4-(2-hydroxyethyl)-1-piperazineethanesulfonic acid (HEPES, 99.9%), NaCl, anhydrous $CaCl_2$, spectrometric grade chloroform and methanol were purchased from Sigma-Aldrich, Saint-Quentin-Fallavier, France. At room temperature DPPC is in a gel-like state (transition temperature ± 41°C) whereas POPC, containing unsaturated hydrocarbon chains, is in a liquid disordered state (transition temperature ± -2°C).

Molecular dynamic simulations

All-atom molecular dynamics (MD) simulations of a lipid bilayer constituted of 356 POPC lipids, disposed in two symmetric leaflets of 178 unit each, was performed in the presence of either the AIM 2 or the AIM 3 compound. The lipid bilayer was solvated using 3000 water molecules, 71 K^+ and 73 Cl^- ions were added to mimic physiological salt conditions and to assure electroneutrality as AIM 2/3 holds a +2 charge, periodic boundary conditions (PBC) were used throughout. The production equilibrium dynamic was preceded by 36 ns of constrained equilibration, to allow for the bilayer relaxation, and was propagated for 200 ns. Having observed no spontaneous penetration of AIM into the bilayer lipid core, we proceeded to 4 ns of steered MD, using the Colvar module,[61] to force the positioning of AIM 2 and AIM 3 at the center of the bilayer. This step was followed by unconstrained MD to observe the continued evolution of the system. Different MD replica starting from different initial conditions have been performed to assure a good sampling of the conformational space. MD simulations were run in the constant pressure and temperature (NPT) ensemble at 300 K and 1 atm, using NAMD code,[62] while the

results have been visualized and analysed using VMD,[63] AMBER lipid force field[64] was used to describe the POPC, while TIP3P model[65] has been chosen for water molecules. The AIM 2 and AIM 3 force field was built based on generalized AMBER force field (gaff)[66] as describe in our previous work.[20]

Supported Lipid Bilayer preparation for AFM experiments

Prior to the build-up of the SLB mimicking cell membrane, unilamellar liposomes of DPPC and POPC were prepared by dissolving the lipids in chloroform and then depositing them on the wall of a rotating round bottom vial under a stream of nitrogen gas. Subsequently, each vial was kept under vacuum overnight, to avoid any trace presence of chloroform, and filled with 5 mL of HEPES-Ca buffer (10 mM HEPES, 150 mM NaCl, 1 mM $CaCl_2$, pH 7.4) to obtain lipids suspension with a concentration of 1 mM. Suspension of small unilamellar vesicles (SUVs) was obtained by sonication of the lipid solution until clear (3 cycles of 2 min each) using a 500 W probe sonicator at 35% of the maximal power (VibraCell 505, VWR International S.A.S, Fontenay-sous-Bois, France). During this procedure the suspension was kept on ice to limit heating and lipid denaturation. Finally, the SUVs suspension was filtered through 0.2 µm pore nylon filters to eliminate titanium particles and then stored at 4˚C until use (storage never exceed 7 days). Supported DPPC/POPC (3:1, v/v) bilayers were obtained by the vesicle fusion method. [67–69] The prepared suspensions of liposomes were left to spontaneously deposit onto a freshly cleaved mica surface mounted into the AFM fluid cell (preheated at 65°C) by incubating the liposome solutions at 65 ˚C for 45 min. Preheated (65°C) HEPES buffer (10 mM HEPES, 150 mM NaCl, pH 7.4) was then added into the AFM fluid cell, and was gradually allowed to cool to room temperature and then rinsed 3 times with HEPES buffer before the AFM experiments.

AFM real-time imaging of SLB were performed with a Bioscope Resolve (Bruker France SAS, Palaiseau, France) operating in PeakForce-Quantitative Nano-Mechanical (PeakForce QNM) imaging mode. Topography images were performed in HEPES buffer at 25°C with a resolution of 512 × 512 pixels, a scan rate of 0.8 Hz, a maximal applied force of 0.25 nN and using silicon nitride AFM-tips with a nominal spring constant of 0.12 N/m (PeakForce-HIRS-SSB tips, Bruker France SAS). Real-time imaging sequences were performed in independent triplicates by recording SLBs images every 15 minutes.

Cell Culture

The MCF 10A (human breast epithelial, ATCC CRL-10317) and MDA-MB-231 (human breast epithelial adenocarcinoma, ATCC HTB-26) immortalized cell lines were purchased from the American Type Culture Collection (ATCC). For our experiments, the MCF 10A cell line was considered non-tumorigenic and acted as the counterpart to the triple negative, metastatic and tumorigenic MDA-MB-231 cells. MCF 10A cells were grown in DMEM/Nutrient Mix F-12 (Gibco, Thermo Fisher Scientific, Illkirch, France) with phenol red and supplemented with 5 % (v/v) horse serum (Gibco, Thermo Fisher Scientific, Illkirch, France), epidermal growth factor 20 ng/mL (Merck, Sigma-Aldrich, Saint-Quentin-Fallavier, France), insulin 10 µg/mL (Merck, Sigma-Aldrich, Saint-Quentin-Fallavier, France), hydrocortisone 0.5 µg/mL (Merck, Sigma-Aldrich, Saint-Quentin-Fallavier, France), cholera toxin 100 ng/mL (Merck, Sigma-Aldrich, Saint-Quentin-Fallavier, France), and 1 % 10 000U penicillin/mL and 10 mg streptomycin/mL (Merck, Sigma-Aldrich, Saint-Quentin-Fallavier, France). MDA-MB-231 cells were grown in RPMI 1640 without phenol red (Gibco, Thermo Fisher Scientific, Illkirch, France) supplemented with 10 % (v/v) fetal calf serum (Merck, Sigma-Aldrich, Saint-Quentin-Fallavier, France), 1 % 10 000U

penicillin/mL and 10 mg streptomycin/mL, and 2 mM L-glutamine (Merck, Sigma-Aldrich, Saint-Quentin-Fallavier, France). Both cell lines were maintained at 37◦C in a humidified atmosphere of 5 % CO_2 and were regularly tested for *Mycoplasma* sp. during experimentation.

Nanomechanical and morphological characterization of cells by AFM

To visualize and quantify the effect of AIM 2 and AIM 3 on the stiffness and outer morphology of the cell's AFM analyses were performed. Nanomechanical and morphological measurements were performed in a liquid environment using a Bioscope Resolve (Bruker Nano Surface, Bruker France S.A.S, Palaiseau, France) and a MFP3D-BIO instrument (Asylum Research Technology, Oxford Instruments Company, Wiesbaden, Germany) respectively.

Biomechanical properties of cells were obtained by nanoindentation technique using silicon nitride cantilevers purchased from Bruker (MLCT, Bruker France S.A.S, Palaiseau, France) with spring constant of about 0.01 $nN.nm^{-1}$ at indentation rate of 1 $\mu m.s^{-1}$. MCF 10A and MDA-MB-231 cells were seeded at a density of 4 x 10^4 or 1.5 x 10^5 cells/mL respectively in 10 cm cell culture plates (Nunclon Delta Surface, Thermo Fisher Scientific, Roskilde, Denmark) and incubated overnight to allow cell attachment. Cells were treated with 2 µM (w/v) of AIM 2 or AIM 3, a dosage previously determined to induce significant effects on the proliferative ability of MCF 10A cells, [20] and incubated for 24 or 96 h. The nanoindentation technique was performed in the appropriate warmed cell culture medium by recording at least 3 Force-Volume Images (FVI) at different locations of the petri dish containing at least 6 to 8 cells. Each FVI consisted of a grid of 50 ×50 force curves measured adopting a 1 $\mu m.s^{-1}$ approach rate of the tip toward the sample. The cell stiffness (Young's modulus) *E* was evaluated by analysing the force-indentation curves within

the framework of the Sneddon model [70,71]. In this model, the Young's modulus is related to the applied force according to the equation (1) given below:

$$F = \frac{2E \cdot \mathrm{Tan}(\alpha)}{\pi(1-\nu^2)} \mathrm{R}^{1/2} \delta^2 \cdot f_{\mathrm{BECC}} \quad (1)$$

where δ is the indentation depth, ν the Poisson coefficient, α the semi-top angle of the conical tip and f_{BECC} is the bottom effect cone correction function that considers the stiffness of the petri dish substrate supporting the cells. All FVI were analysed using an automatic MATLAB (The MathWorks Inc., Natick, MA, USA) algorithm detailed elsewhere [72] and the average and median Young's moduli values given in this work were derived from at least 1000 force curves.

For the morphological analyses, MCF 10A and MDA-MB-231 cells were seeded at a density of 4 x 10^4 or 1.5 x 10^5 cells/mL respectively in 6 cm cell culture plates (Nunclon Delta Surface, Thermo Fisher Scientific, Roskilde, Denmark) and incubated overnight to allow for cell attachment. Subsequently, cells were treated with 2 µM (w/v) of AIM 2 or AIM 3 and incubated for 24 or 96 h. The cell monolayers were fixed with 4 % (w/v) paraformaldehyde (Electron Microscopy Sciences, Hatfield, PA, USA) for 20 min and washed with PBS (phosphate buffered saline; Gibco, Thermo Fisher Scientific, Illkirch, France). Cell topography was obtained by AFM operating in peak-force tapping™ mode using silicon nitride cantilevers purchased from Bruker (PeakForce-HIRS-SSB, Bruker France S.A.S, Palaiseau, France) with spring constant of about 0.12 nN.nm^{-1} and all images were recorded with a resolution of 512 × 512 pixels for a scan rate of 0.5 Hz.

Analysis of cell size and granulometry using flow cytometry

To quantify the effect of AIM 2 and AIM 3 on the size and granulometry of the cells, flow cytometry analyses were performed on the cell lines. MCF 10A and MDA-MB-231 cells were seeded at a density of 4 x 10^4 or 1.5 x 10^5 cells/mL respectively into 6-well cell culture plates (Sarstedt, Nümbrecht, Germany) and incubated overnight to allow for cell attachment. Subsequently, cells were treated with 2 µM (w/v) of AIM 2 or AIM 3 and incubated for 24 or 96 h. The flow cytometry instrument sorted the cells by size and granulometry and required no prior staining. Thus, prior to acquisition, cells in each condition was washed three times in PBS, harvested by 0.05 % trypsin/EDTA (Gibco, Thermo Fisher Scientific, Illkirch, France) and centrifuged for 5 min at 1100 rpm to form a pellet. Following supernatant aspiration, the cells were gently resuspended in 300 µL of PBS and immediately analyzed using a Cytoflex cytometer (Beckman Coulter, Villepinte, France). Twenty thousand events in the population of cells were detected depending on their size (forward scatter, FSC) and granulometry (side scatter, SSC) gating, whilst the cells outside the gate were excluded (FSC-Height/FSC-Area gate). Each experiment was performed in triplicate and the data was analyzed using the CytExpert 2.3 software (Beckman Coulter, Villepinte, France).

Immunofluorescence microscopy

To visualize the internal effect of AIM 2 and AIM 3 on the cells, immunofluorescent microscopy experiments were performed on the cell lines. MCF 10A and MDA-MB-231 cells were seeded at a density of 4 x 10^4 or 1.5 x 10^5 cells/mL respectively onto glass coverslips placed in 6 cm cell culture plates (Nunclon Delta Surface, Thermo Fisher Scientific, Roskilde, Denmark) and incubated overnight to allow for cell attachment. Subsequently, cells were treated with 2 µM (w/v) of AIM 2 or AIM 3 for 24 or 96 h. The cell monolayers growing on the glass coverslips were

fixed with 4 % (w/v) paraformaldehyde for 20 min, washed with PBS, and permeabilized with 0.2 % Triton X-100 (Merck, Sigma-Aldrich, Saint-Quentin-Fallavier, France) and 3 % bovine serum albumin (BSA; Merck, Sigma-Aldrich, Saint-Quentin-Fallavier, France) in PBS for 30 min at room temperature. Cells were incubated with rabbit anti-α-tubulin monoclonal antibody (Ab52866; Abcam, Paris, France) diluted 1:500 (v/v), and purified mouse anti-Cytochrome c monoclonal antibody (556432; BD Biosciences, San Jose, CA, USA) diluted 1:400 (v/v) in PBS containing 0.2 % Triton X-100 and 3 % BSA for 45 min to label the α-tubulin within the cytoskeleton and the cytochrome c of the mitochondria. After washing with PBS containing 0.2 % Triton X-100 and 3 % BSA, cells were stained with fluorescein F(ab')2 fragment of goat anti-rabbit IgG (A10526; Molecular Probes, Thermo Fisher Scientific, Illkirch, France) and goat anti-mouse Alexa Fluor 594 secondary antibodies (A11032; Molecular Probes, Thermo Fisher Scientific, Illkirch, France) diluted 1:200 (v/v) in PBS containing 0.2 % Triton X-100 and 3 % BSA for 30 min. Cells were also incubated with Alexa Fluor 594 Phalloidin (A12381; Thermo Fisher Scientific, Illkirch, France) diluted 1:30 (v/v) in PBS containing 0.2 % Triton X-100 and 3 % BSA for 45 min to visualize the F-actin of the cytoskeleton. For all experiments the nuclei were counterstained with Hoechst 33342 dye (Invitrogen, Thermo Fisher Scientific, Illkirch, France), diluted 1:10 000 (v/v) in PBS, for 10 min. After washing twice with PBS containing 0.2 % Triton X-100 and 3 % BSA, cells were mounted onto glass slides using FluorSave Reagent (Calbiochem, Sigma-Aldrich, Saint-Quentin-Fallavier, France) and was observed with an epifluorescence microscope (Nikon Eclipse 80i, Melville, NY, USA) with a ×40 and ×100 oil immersion objective (Nikon, Melville, NY, USA). Images were collected with a digital camera (Nikon, DS-Ri1, Mellville, NY, USA).

Statistical analysis

GraphPad Prism 7 software (GraphPad Prism Software Inc., San Diego, CA, USA) was used for all statistical analyses. To evaluate the Young's modulus for each cell line in each treatment and non-treated group, 10 – 15 cells were examined, and up to 200 force-displacement curves were obtained. The mean and median ± standard deviation (SD) values were calculated and analyzed by a Kruskal-Wallis one-way analysis of variance (ANOVA) to compare the cellular stiffness effect of AIM 2/3 treatment on both cell lines. In all box plots, the boxes represent the interquartile range between first and third quartiles, whereas the whiskers represent the 95% and 5% values, and the squares represent the average. To evaluate the effect of AIM 2/3 on the cell lines' size and granulometry over time using flow cytometry, three independent experiments were performed with 20 000 cells analyzed in each sample. The flow cytometry determined median values were analyzed by a two-way ANOVA with a Tukey's comparison test. An alpha level of 0.05 was set for all tests (95 % confidence interval), and the level of statistical difference was considered as not significant at $P > 0.05$ (ns), and significant from $P \leq 0.05$ (*), $P \leq 0.01$ (**) to $P \leq 0.001$ (***). P values with ≤ 0.0001 were denoted as ***.

SUPPRTIG INFORMATION

Figure S1. UV-vis spectroscopy data concerning the aggregation of AIM 2 and AIM 3 at different volumes of fetal bovine serum (FBS).

Figure S2. AFM images monitoring the real time evolution of DPPC/POPC SLB under the effects of either AIM 2 or AIM 3 after 0, 30 and 60 mins. Vertical cross-section indicating height measured at dashed line of images. Image scale bar is set to 4 μm.

Figure S3. Representative force curves recorded on MCF 10A and MDA-MB-231 cells after 24 h without metallodrug treatment (a – c), after 24 h treatment with 2 μM AIM 2h (d – f) and after 24 h treatment with 2 μM AIM 3 (b, e). Circles corresponds to experimental data and the red lines to the theoretical fittings derived from Sneddon Model according to algorithm developed by Polyakov et al.

Description of wound healing assay methodology.

Figure S4. Wound healing scratch test assay images of MCF 10A (a – l) and MDA-MB-231 (m – x) cells after 24 h of AIM 2 or AIM 3 pre-treatments at 40X magnification. The ability of the cells to migrate, after a scratch was applied to the monolayer, was monitored immediately after at 0, 6, 24 and 48 h.

Figure S5. Wound healing scratch test assay images of MCF 10A (a – l) and MDA-MB-231 (m – x) cells after 72 h of AIM 2 or AIM 3 pre-treatments at 40X magnification. The ability of the cells to migrate, after a scratch was applied to the monolayer, was monitored immediately after at 0, 6, 24 and 48 h.

AUTHOR INFORMATION

Corresponding Authors

*antonio.monari@univ-lorraine.fr, stephanie.grandemange@univ-lorraine.fr, nadege.touche@univ-lorraine.fr, gregory.francius@univ-lorraine.fr

Author Contributions

The manuscript was written with contributions from all authors. All authors have given approval to the final version of the manuscript. †These authors contributed equally to this work.

Acknowledgements

The authors would like to acknowledge the Lorraine Université d'Excellence (LUE) and the Spectroscopy and Microscopy Service Facility (SMI) of LCPME (Université de Lorraine-CNRS – http://www.lcpme.cnr-nancy.fr) for AFM analyses. MD simulations have been performed using the LPCT local computer resources.

Abbreviations

AFM, atomic force microscopy; AIM, anti-cancer iron molecule; ANOVA, one-way analysis of variance; ATCC, American Type Cell Culture; BSA, bovine serum albumin; DPPC, 1,2-dipalmitoyl-sn-glycero-3-phosphocholine; FSC, forward scatter; FVI, force volume images; HEPES, 4-(2-hydroxyethyl)-1-piperazineethanesulfonic acid; MCF 10A, epithelial non-tumorigenic breast cell line; MD, molecular dynamics; MDA-MB-231, epithelial tumorigenic breast cell line; NPT, constant pressure and temperature; PBC, periodic boundary conditions; PBS, phosphate buffered saline; POPC, 1-palmitoyl-2-oleoyl-glycero-3-phosphocholine; SD, standard deviation; SLB, supported lipid bilayer; SSC, side scatter; SUVs, small unilamellar vesicles.

References

(1) Florea, A.-M.; Büsselberg, D. Cisplatin as an Anti-Tumor Drug: Cellular Mechanisms of Activity, Drug Resistance and Induced Side Effects. *Cancers 2011, Vol. 3, Pages 1351-1371* **2011**, *3* (1), 1351–1371. https://doi.org/10.3390/CANCERS3011351.

(2) Galluzzi, L.; Vitale, I.; Michels, J.; Brenner, C.; Szabadkai, G.; Harel-Bellan, A.; Castedo, M.; Kroemer, G. Systems Biology of Cisplatin Resistance: Past, Present and Future. *Cell Death Dis. 2014 55* **2014**, *5* (5), e1257–e1257. https://doi.org/10.1038/cddis.2013.428.

(3) Ghosh, S. Cisplatin: The First Metal Based Anticancer Drug. *Bioorg. Chem.* **2019**, *88*. https://doi.org/10.1016/J.BIOORG.2019.102925.

(4) Yan, Y. K.; Melchart, M.; Habtemariam, A.; Sadler, P. J. Organometallic Chemistry, Biology and Medicine: Ruthenium Arene Anticancer Complexes. *Chem. Commun.* **2005**, No. 38, 4764. https://doi.org/10.1039/b508531b.

(5) Kostova, I. Ruthenium Complexes as Anticancer Agents. *Curr. Med. Chem.* **2006**, *13* (9), 1085–1107. https://doi.org/10.2174/092986706776360941.

(6) Lazarević, T.; Rilak, A.; Bugarčić, Ž. D. Platinum, Palladium, Gold and Ruthenium Complexes as Anticancer Agents: Current Clinical Uses, Cytotoxicity Studies and Future Perspectives. *European Journal of Medicinal Chemistry*. Elsevier Masson SAS December 15, 2017, pp 8–31. https://doi.org/10.1016/j.ejmech.2017.04.007.

(7) Bouché, M.; Hognon, C.; Grandemange, S.; Monari, A.; Gros, P. C. Recent Advances in Iron-Complexes as Drug Candidates for Cancer Therapy: Reactivity, Mechanism of Action and Metabolites. *Dalt. Trans.* **2020**, *49* (33), 11451–11466.

https://doi.org/10.1039/d0dt02135k.

(8) Fiorina, V. J.; Dubois, R. J.; Brynes, S. Ferrocenyl Polyamines as Agents for the Chemoimmunotherapy of Cancer. *J. Med. Chem.* **1978**, *21* (4), 393–395. https://doi.org/10.1021/JM00202A016.

(9) Wang, R.; Chen, H.; Yan, W.; Zheng, M.; Zhang, T.; Zhang, Y. Ferrocene-Containing Hybrids as Potential Anticancer Agents: Current Developments, Mechanisms of Action and Structure-Activity Relationships. *Eur. J. Med. Chem.* **2020**, *190*, 112109. https://doi.org/10.1016/J.EJMECH.2020.112109.

(10) Shoukat, H.; Altaf, A. A.; Badshah, A. Ferrocene-Based Metallodrugs. *Adv. Met.* **2020**, 115–136. https://doi.org/10.1002/9781119640868.CH4.

(11) Hillard, E.; Vessières, A.; Thouin, L.; Jaouen, G.; Amatore, C. Ferrocene-Mediated Proton-Coupled Electron Transfer in a Series of Ferrocifen-Type Breast-Cancer Drug Candidates. *Angew. Chemie Int. Ed.* **2005**, *45* (2), 285–290. https://doi.org/10.1002/ANIE.200502925.

(12) Nguyen, A.; Vessières, A.; Hillard, E. A.; Top, S.; Pigeon, P.; Jaouen, G. Ferrocifens and Ferrocifenols as New Potential Weapons against Breast Cancer. *Chimia (Aarau).* **2007**, *61* (11), 716–724. https://doi.org/10.2533/CHIMIA.2007.716.

(13) Pigeon, P.; Top, S.; Vessières, A.; Huché, M.; Görmen, M.; Arbi, M. El; Plamont, M.-A.; McGlinchey, M. J.; Jaouen, G. A New Series of Ferrocifen Derivatives, Bearing Two Aminoalkyl Chains, with Strong Antiproliferative Effects on Breast Cancer Cells. *New J. Chem.* **2011**, *35* (10), 2212–2218. https://doi.org/10.1039/C1NJ20192A.

(14) Cunningham, L.; Wang, Y.; Nottingham, C.; Pagsulingan, J.; Jaouen, G.; McGlinchey, M.

J.; Guiry, P. J. Enantioselective Synthesis of Planar Chiral Ferrocifens That Show Chiral Discrimination in Antiproliferative Activity on Breast Cancer Cells. *ChemBioChem* **2020**, *21* (20), 2974–2981. https://doi.org/10.1002/CBIC.202000311.

(15) Ornelas, C. Application of Ferrocene and Its Derivatives in Cancer Research. *New J. Chem.* **2011**, *35* (10), 1973–1985. https://doi.org/10.1039/C1NJ20172G.

(16) Patra, M.; Gasser, G. The Medicinal Chemistry of Ferrocene and Its Derivatives. *Nat. Rev. Chem. 2017 19* **2017**, *1* (9), 1–12. https://doi.org/10.1038/s41570-017-0066.

(17) Mejía, C.; Ortega-Rosales, S.; Ruiz-Azuara, L. Mechanism of Action of Anticancer Metallodrugs. In *Biomedical Applications of Metals*; Springer International Publishing, 2018; pp 213–234. https://doi.org/10.1007/978-3-319-74814-6_10.

(18) Spinello, A.; Magistrato, A. An Omics Perspective to the Molecular Mechanisms of Anticancer Metallo-Drugs in the Computational Microscope Era. *Expert Opinion on Drug Discovery*. Taylor and Francis Ltd August 3, 2017, pp 813–825. https://doi.org/10.1080/17460441.2017.1340272.

(19) Wang, H.; Zhou, Y.; Xu, X.; Li, H.; Sun, H. Metalloproteomics in Conjunction with Other Omics for Uncovering the Mechanism of Action of Metallodrugs: Mechanism-Driven New Therapy Development. *Current Opinion in Chemical Biology*. Elsevier Ltd April 1, 2020, pp 171–179. https://doi.org/10.1016/j.cbpa.2020.02.006.

(20) Gattuso, H.; Duchanois, T.; Besancenot, V.; Barbieux, C.; Assfeld, X.; Becuwe, P.; Gros, P. C.; Grandemange, S.; Monari, A. Interaction of Iron II Complexes with B-DNA. Insights from Molecular Modeling, Spectroscopy, and Cellular Biology. *Front. Chem.* **2015**, *3*

(DEC), 67. https://doi.org/10.3389/fchem.2015.00067.

(21) Notaro, A.; Gasser, G.; Castonguay, A. Note of Caution for the Aqueous Behaviour of Metal-Based Drug Candidates. *ChemMedChem* **2020**, *15* (4), 345–348. https://doi.org/10.1002/CMDC.201900677.

(22) Debnath, J.; Muthuswamy, S. K.; Brugge, J. S. Morphogenesis and Oncogenesis of MCF-10A Mammary Epithelial Acini Grown in Three-Dimensional Basement Membrane Cultures. *Methods*. Academic Press Inc. July 1, 2003, pp 256–268. https://doi.org/10.1016/S1046-2023(03)00032-X.

(23) Jeong, Y. J.; Kang, J. S.; Lee, S. I.; Son, D. M.; Yun, J.; Baek, J. Y.; Kim, S. K.; Lee, K.; Park, S. K. Breast Cancer Cells Evade Paclitaxel-Induced Cell Death by Developing Resistance to Dasatinib. *Oncol. Lett.* **2016**, *12* (3), 2153–2158. https://doi.org/10.3892/ol.2016.4852.

(24) Cailleau, R.; Mackay, B.; Young, R. K.; Reeves, W. J. Tissue Culture Studies on Pleural Effusions from Breast Carcinoma Patients. *Cancer Res.* **1974**, *34* (4).

(25) Guck, J.; Schinkinger, S.; Lincoln, B.; Wottawah, F.; Ebert, S.; Romeyke, M.; Lenz, D.; Erickson, H. M.; Ananthakrishnan, R.; Mitchell, D.; Kas, J.; Ulvick, S.; Bilby, C. Optical Deformability as an Inherent Cell Marker for Testing Malignant Transformation and Metastatic Competence. *Biophys. J.* **2005**, *88* (5), 3689–3698. https://doi.org/10.1529/biophysj.104.045476.

(26) Butcher, D. T.; Alliston, T.; Weaver, V. M. A Tense Situation: Forcing Tumour Progression. *Nature Reviews Cancer*. Nature Publishing Group February 2009, pp 108–122.

https://doi.org/10.1038/nrc2544.

(27) Nagelkerke, A.; Bussink, J.; Rowan, A. E.; Span, P. N. The Mechanical Microenvironment in Cancer: How Physics Affects Tumours. *Semin. Cancer Biol.* **2015**, *35*, 62–70. https://doi.org/10.1016/J.SEMCANCER.2015.09.001.

(28) Lin, H.-H.; Lin, H.-K.; Lin, I.-H.; Chiou, Y.-W.; Chen, H.-W.; Liu, C.-Y.; Harn, H. I.-C.; Chiu, W.-T.; Wang, Y.-K.; Shen, M.-R.; Tang, M.-J. Mechanical Phenotype of Cancer Cells: Cell Softening and Loss of Stiffness Sensing. *Oncotarget* **2015**, *6* (25), 20946. https://doi.org/10.18632/ONCOTARGET.4173.

(29) Lekka, M. Discrimination Between Normal and Cancerous Cells Using AFM. *BioNanoScience 2016 61* **2016**, *6* (1), 65–80. https://doi.org/10.1007/S12668-016-0191-3.

(30) Dutta, D.; Schmidt, R.; Fernando, S. C.; Dastider, I. G. A Comparative Study of Force Measurements in Solution Using Micron and Nano Size Probe. *World J. Nano Sci. Eng.* **2019**, *09* (01), 1–14. https://doi.org/10.4236/wjnse.2019.91001.

(31) Berquand, A.; Mingeot-Leclercq, M. P.; Dufrêne, Y. F. Real-Time Imaging of Drug–Membrane Interactions by Atomic Force Microscopy. *Biochim. Biophys. Acta - Biomembr.* **2004**, *1664* (2), 198–205. https://doi.org/10.1016/J.BBAMEM.2004.05.010.

(32) Calzado-Martín, A.; Encinar, M.; Tamayo, J.; Calleja, M.; San Paulo, A. Effect of Actin Organization on the Stiffness of Living Breast Cancer Cells Revealed by Peak-Force Modulation Atomic Force Microscopy. *ACS Nano* **2016**, *10* (3), 3365–3374. https://doi.org/10.1021/acsnano.5b07162.

(33) Dutta, D.; Palmer, X. L.; Ortega-Rodas, J.; Balraj, V.; Dastider, I. G.; Chandra, S.

Biomechanical and Biophysical Properties of Breast Cancer Cells Under Varying Glycemic Regimens. *Breast Cancer Basic Clin. Res.* **2020**, *14*. https://doi.org/10.1177/1178223420972362.

(34) Lincoln, B.; Erickson, H. M.; Schinkinger, S.; Wottawah, F.; Mitchell, D.; Ulvick, S.; Bilby, C.; Guck, J. Deformability-Based Flow Cytometry. *Cytom. Part A* **2004**, *59* (2), 203–209. https://doi.org/10.1002/cyto.a.20050.

(35) Lekka, M.; Laidler, P.; Gil, D.; Lekki, J.; Stachura, Z.; Hrynkiewicz, A. Z. Elasticity of Normal and Cancerous Human Bladder Cells Studied by Scanning Force Microscopy. *Eur. Biophys. J.* **1999**, *28* (4), 312–316. https://doi.org/10.1007/s002490050213.

(36) Zhao, J.; Zhang, J.; Yu, M.; Xie, Y.; Huang, Y.; Wolff, D. W.; Abel, P. W.; Tu, Y. Mitochondrial Dynamics Regulates Migration and Invasion of Breast Cancer Cells. *Oncogene* **2013**, *32* (40), 4814–4824. https://doi.org/10.1038/onc.2012.494.

(37) Daniel, R.; Mengeta, A.; Bilodeau, P.; Lee, J. M. Mitochondria Tether to Focal Adhesions during Cell Migration and Regulate Their Size. *bioRxiv*. bioRxiv November 1, 2019, p 827998. https://doi.org/10.1101/827998.

(38) Agus, D. B.; Alexander, J. F.; Arap, W.; Ashili, S.; Aslan, J. E.; Austin, R. H.; Backman, V.; Bethel, K. J.; Bonneau, R.; Chen, W. C.; Chen-Tanyolac, C.; Choi, N. C.; Curley, S. A.; Dallas, M.; Damania, D.; Davies, P. C. W.; Decuzzi, P.; Dickinson, L.; Estevez-Salmeron, L.; Estrella, V.; Ferrari, M.; Fischbach, C.; Foo, J.; Fraley, S. I.; Frantz, C.; Fuhrmann, A.; Gascard, P.; Gatenby, R. A.; Geng, Y.; Gerecht, S.; Gillies, R. J.; Godin, B.; Grady, W. M.; Greenfield, A.; Hemphill, C.; Hempstead, B. L.; Hielscher, A.; Hillis, W. D.; Holland, E. C.; Ibrahim-Hashim, A.; Jacks, T.; Johnson, R. H.; Joo, A.; Katz, J. E.; Kelbauskas, L.;

Kesselman, C.; King, M. R.; Konstantopoulos, K.; Kraning-Rush, C. M.; Kuhn, P.; Kung, K.; Kwee, B.; Lakins, J. N.; Lambert, G.; Liao, D.; Licht, J. D.; Liphardt, J. T.; Liu, L.; Lloyd, M. C.; Lyubimova, A.; Mallick, P.; Marko, J.; McCarty, O. J. T.; Meldrum, D. R.; Michor, F.; Mumenthaler, S. M.; Nandakumar, V.; O'Halloran, T. V.; Oh, S.; Pasqualini, R.; Paszek, M. J.; Philips, K. G.; Poultney, C. S.; Rana, K.; Reinhart-King, C. A.; Ros, R.; Semenza, G. L.; Senechal, P.; Shuler, M. L.; Srinivasan, S.; Staunton, J. R.; Stypula, Y.; Subramanian, H.; Tlsty, T. D.; Tormoen, G. W.; Tseng, Y.; Van Oudenaarden, A.; Verbridge, S. S.; Wan, J. C.; Weaver, V. M.; Widom, J.; Will, C.; Wirtz, D.; Wojtkowiak, J.; Wu, P. H. A Physical Sciences Network Characterization of Non-Tumorigenic and Metastatic Cells. *Sci. Rep.* **2013**, *3*. https://doi.org/10.1038/srep01449.

(39) Santidrian, A. F.; Matsuno-Yagi, A.; Ritland, M.; Seo, B. B.; LeBoeuf, S. E.; Gay, L. J.; Yagi, T.; Felding-Habermann, B. Mitochondrial Complex I Activity and NAD+/NADH Balance Regulate Breast Cancer Progression. *J. Clin. Invest.* **2013**, *123* (3), 1068–1081. https://doi.org/10.1172/JCI64264.

(40) Biel, T. G.; Aryal, B.; Gerber, M. H.; Trevino, J. G.; Mizuno, N.; Rao, V. A. Mitochondrial Dysfunction Generates Aggregates That Resist Lysosomal Degradation in Human Breast Cancer Cells. *Cell Death Dis.* **2020**, *11* (6), 460. https://doi.org/10.1038/s41419-020-2658-y.

(41) Bergamo, A.; Masi, A.; Dyson, P. J.; Sava, G. Modulation of the Metastatic Progression of Breast Cancer with an Organometallic Ruthenium Compound. *Int. J. Oncol.* **2008**, *33* (6), 1281–1289. https://doi.org/10.3892/ijo_00000119.

(42) Dhivya, R.; Jaividhya, P.; Riyasdeen, A.; Palaniandavar, M.; Mathan, G.; Akbarsha, M. A.

In Vitro Antiproliferative and Apoptosis-Inducing Properties of a Mononuclear Copper(II) Complex with Dppz Ligand, in Two Genotypically Different Breast Cancer Cell Lines. *BioMetals* **2015**, *28* (5), 929–945. https://doi.org/10.1007/s10534-015-9877-1.

(43) Lee, R. F. S.; Escrig, S.; Maclachlan, C.; Knott, G. W.; Meibom, A.; Sava, G.; Dyson, P. J. The Differential Distribution of RAPTA-T in Non-Invasive and Invasive Breast Cancer Cells Correlates with Its Anti-Invasive and Anti-Metastatic Effects. *Int. J. Mol. Sci.* **2017**, *18* (9), 1869. https://doi.org/10.3390/ijms18091869.

(44) Irace, C.; Misso, G.; Capuozzo, A.; Piccolo, M.; Riccardi, C.; Luchini, A.; Caraglia, M.; Paduano, L.; Montesarchio, D.; Santamaria, R. Antiproliferative Effects of Ruthenium-Based Nucleolipidic Nanoaggregates in Human Models of Breast Cancer in Vitro: Insights into Their Mode of Action. *Sci. Rep.* **2017**, *7* (1), 1–13. https://doi.org/10.1038/srep45236.

(45) Pracharova, J.; Novohradsky, V.; Kostrhunova, H.; Štarha, P.; Trávníček, Z.; Kasparkova, J.; Brabec, V. Half-Sandwich Os(Ii) and Ru(Ii) Bathophenanthroline Complexes: Anticancer Drug Candidates with Unusual Potency and a Cellular Activity Profile in Highly Invasive Triple-Negative Breast Cancer Cells. *Dalt. Trans.* **2018**, *47* (35), 12197–12208. https://doi.org/10.1039/C8DT02236D.

(46) Kostrhunova, H.; Zajac, J.; Novohradsky, V.; Kasparkova, J.; Malina, J.; Aldrich-Wright, J. R.; Petruzzella, E.; Sirota, R.; Gibson, D.; Brabec, V. A Subset of New Platinum Antitumor Agents Kills Cells by a Multimodal Mechanism of Action Also Involving Changes in the Organization of the Microtubule Cytoskeleton. *J. Med. Chem.* **2019**, *62* (10), 5176–5190. https://doi.org/10.1021/acs.jmedchem.9b00489.

(47) Mejía, C.; Ortega-Rosales, S.; Ruiz-Azuara, L. Mechanism of Action of Anticancer

Metallodrugs. *Biomed. Appl. Met.* **2018**, 213–234. https://doi.org/10.1007/978-3-319-74814-6_10.

(48) Casini, A.; Reedijk, J. Interactions of Anticancer Pt Compounds with Proteins: An Overlooked Topic in Medicinal Inorganic Chemistry? *Chem. Sci.* **2012**, *3* (11), 3135–3144. https://doi.org/10.1039/C2SC20627G.

(49) Todd, R. C.; Lippard, S. J. Inhibition of Transcription by Platinum Antitumor Compounds. *Metallomics* **2009**, *1* (4), 280–291. https://doi.org/10.1039/B907567D.

(50) Burger, H.; Loos, W.; Eechoute, K.; Verweij, J.; Mathijssen, R.; Wiemer, E. Drug Transporters of Platinum-Based Anticancer Agents and Their Clinical Significance. *Drug Resist. Updat.* **2011**, *14* (1), 22–34. https://doi.org/10.1016/J.DRUP.2010.12.002.

(51) Johnstone, T. C.; Suntharalingam, K.; Lippard, S. J. The Next Generation of Platinum Drugs: Targeted Pt(II) Agents, Nanoparticle Delivery, and Pt(IV) Prodrugs. *Chem. Rev.* **2016**, *116* (5), 3436–3486. https://doi.org/10.1021/ACS.CHEMREV.5B00597.

(52) Pinheiro Araujo, T.; Gandin, V.; Kavanagh, P.; Braude, J. P.; Nodari, L.; Montagner, D.; Erxleben, A. DNA Binding, Cleavage and Cytotoxicity of a Novel Dimetallic Fe(III) Triaza-Cyclononane Complex. *Inorganica Chim. Acta* **2016**, *452*, 170–175. https://doi.org/10.1016/J.ICA.2016.02.044.

(53) Kafer, A.; Krug, H. F. The Effect of Organometals on Cellulr Shape and Cell Cycle. *Main Gr. Met. Chem.* **1997**, *20* (1), 19–26. https://doi.org/10.1515/MGMC.1997.20.1.19.

(54) Schiff, P.; Fant, J.; Horwitz, S. Promotion of Microtubule Assembly in Vitro by Taxol. *Nature* **1979**, *277* (5698), 665–667. https://doi.org/10.1038/277665A0.

(55) Guéritte-Voegelein, F.; Guénard, D.; Lavelle, F.; Le Goff, M.; Mangatal, L.; Potier, P. Relationships between the Structure of Taxol Analogues and Their Antimitotic Activity. *J. Med. Chem.* **1991**, *34* (3), 992–998. https://doi.org/10.1021/JM00107A017.

(56) Bostancıoğlu, R. B.; Demirel, S.; Cin, G. T.; Koparal, A. T. Novel Ferrocenyl-Containing N-Acetyl-2-Pyrazolines Inhibit in Vitro Angiogenesis and Human Lung Cancer Growth by Interfering with F-Actin Stress Fiber Polimeryzation. *https://doi.org/10.3109/01480545.2013.776579* **2013**, *36* (4), 484–495. https://doi.org/10.3109/01480545.2013.776579.

(57) Wieczorek, A.; Błauż, A.; Zakrzewski, J.; Rychlik, B.; Plażuk, D. Ferrocenyl 2,5-Piperazinediones as Tubulin-Binding ABCB1 and ABCG2 Inhibitors Activeagainst MDR Cells. *ACS Med. Chem. Lett.* **2016**, *7* (6), 612. https://doi.org/10.1021/ACSMEDCHEMLETT.6B00046.

(58) Pilon, A.; Brás, A. R.; Côrte-Real, L.; Avecilla, F.; Costa, P. J.; Preto, A.; Garcia, M. H.; Valente, A. A New Family of Iron(II)-Cyclopentadienyl Compounds Shows Strong Activity against Colorectal and Triple Negative Breast Cancer Cells. *Mol. 2020, Vol. 25, Page 1592* **2020**, *25* (7), 1592. https://doi.org/10.3390/MOLECULES25071592.

(59) Iacopetta, D.; Ceramella, J.; Rosano, C.; Mariconda, A.; Pellegrino, M.; Sirignano, M.; Saturnino, C.; Catalano, A.; Aquaro, S.; Longo, P.; Sinicropi, M. S. N-Heterocyclic Carbene-Gold(I) Complexes Targeting Actin Polymerization. *Appl. Sci. 2021, Vol. 11, Page 5626* **2021**, *11* (12), 5626. https://doi.org/10.3390/APP11125626.

(60) Acharya, S.; Maji, M.; Chakraborty, M. P.; Bhattacharya, I.; Das, R.; Gupta, A.; Mukherjee, A. Disruption of the Microtubule Network and Inhibition of VEGFR2 Phosphorylation by

Cytotoxic N,O-Coordinated Pt(II) and Ru(II) Complexes of Trimethoxy Aniline-Based Schiff Bases. *Inorg. Chem.* **2021**, *60* (5), 3418–3430. https://doi.org/10.1021/ACS.INORGCHEM.0C03820.

(61) Fiorin, G.; Klein, M. L.; Hénin, J. Using Collective Variables to Drive Molecular Dynamics Simulations. *Mol. Phys.* **2013**, *111* (22–23), 3345–3362. https://doi.org/10.1080/00268976.2013.813594.

(62) Phillips, J. C.; Braun, R.; Wang, W.; Gumbart, J.; Tajkhorshid, E.; Villa, E.; Chipot, C.; Skeel, R. D.; Kalé, L.; Schulten, K. Scalable Molecular Dynamics with NAMD. *Journal of Computational Chemistry*. John Wiley and Sons Inc. 2005, pp 1781–1802. https://doi.org/10.1002/jcc.20289.

(63) Humphrey, W.; Dalke, A.; Schulten, K. VMD: Visual Molecular Dynamics. *J. Mol. Graph.* **1996**, *14* (1), 33–38. https://doi.org/10.1016/0263-7855(96)00018-5.

(64) Weiner, S. J.; Kollman, P. A.; Nguyen, D. T.; Case, D. A. An All Atom Force Field for Simulations of Proteins and Nucleic Acids. *J. Comput. Chem.* **1986**, *7* (2), 230–252. https://doi.org/10.1002/jcc.540070216.

(65) Jorgensen, W. L.; Chandrasekhar, J.; Madura, J. D.; Impey, R. W.; Klein, M. L. Comparison of Simple Potential Functions for Simulating Liquid Water. *J. Chem. Phys.* **1983**, *79* (2), 926–935. https://doi.org/10.1063/1.445869.

(66) Wang, J.; Wang, W.; Kollman, P. A.; Case, D. A. Automatic Atom Type and Bond Type Perception in Molecular Mechanical Calculations. *J. Mol. Graph. Model.* **2006**, *25* (2), 247–260. https://doi.org/10.1016/j.jmgm.2005.12.005.

(67) Leonenko, Z. V.; Carnini, A.; Cramb, D. T. Supported Planar Bilayer Formation by Vesicle Fusion: The Interaction of Phospholipid Vesicles with Surfaces and the Effect of Gramicidin on Bilayer Properties Using Atomic Force Microscopy. *Biochim. Biophys. Acta - Biomembr.* **2000**, *1509* (1–2), 131–147. https://doi.org/10.1016/S0005-2736(00)00288-1.

(68) El Kirat, K.; Morandat, S.; Dufrêne, Y. F. Nanoscale Analysis of Supported Lipid Bilayers Using Atomic Force Microscopy. *Biochimica et Biophysica Acta - Biomembranes*. Elsevier April 1, 2010, pp 750–765. https://doi.org/10.1016/j.bbamem.2009.07.026.

(69) Freudenthal, O.; Quilès, F.; Francius, G.; Wojszko, K.; Gorczyca, M.; Korchowiec, B.; Rogalska, E. Nanoscale Investigation of the Interaction of Colistin with Model Phospholipid Membranes by Langmuir Technique, and Combined Infrared and Force Spectroscopies. *Biochim. Biophys. Acta - Biomembr.* **2016**, *1858* (11), 2592–2602. https://doi.org/10.1016/j.bbamem.2016.07.015.

(70) Sneddon, I. N. The Relation between Load and Penetration in the Axisymmetric Boussinesq Problem for a Punch of Arbitrary Profile. *Int. J. Eng. Sci.* **1965**, *3* (1), 47–57. https://doi.org/10.1016/0020-7225(65)90019-4.

(71) Gavara, N.; Chadwick, R. S. Determination of the Elastic Moduli of Thin Samples and Adherent Cells Using Conical Atomic Force Microscope Tips. *Nat. Nanotechnol.* **2012**, *7* (11), 733–736. https://doi.org/10.1038/nnano.2012.163.

(72) Polyakov, P.; Soussen, C.; Duan, J.; Duval, J. F. L.; Brie, D.; Francius, G. Automated Force Volume Image Processing for Biological Samples. *PLoS One* **2011**, *6* (4), 18887. https://doi.org/10.1371/journal.pone.0018887.